Computational Mechanics manuscript No.
(will be inserted by the editor)

From Process to Property: Multi-physics Modeling of Dislocation Dynamics and Microscale Damage in Metal Additive Manufacturing

Daijun Hu[1,†], Nicolò Grilli[2,†], Wentao Yan[1] ⋆

[1] Department of Mechanical Engineering, National University of Singapore, Singapore 117575, Singapore

[2] Department of Electrical, Electronics and Mechanical Engineering, University of Bristol, BS8 1TR, Bristol, UK

Abstract Metal additive manufacturing (AM) has the potential to tailor the mechanical performance of materials. Due to the complex thermal history and unique microstructure, AM materials are reported to contain distinct dislocation networks with a high dislocation density, which affect the plastic deformation behavior and fracture. However, it is challenging to experimentally observe the formation of such dislocation structures. In this work, a multi-scale multi-physics crystal plasticity modeling framework that integrates the process-structure-property relationship in metal AM is developed. The temperature field obtained from thermal-fluid flow simulations of the AM process and the microstructure from the phase field model of grain growth are combined into thermo-mechanical crystal plasticity simulations to obtain grain-scale thermal stresses. These stresses are used as input to simulate the evolution of dislocation structures within individual grains. Taking AM 316L stainless steel as the material of interest, the effect of initial dislocation configuration on the slip plane and cross-slip mechanism on the dislocation structure formation are investigated. Furthermore, a phase field damage model is implemented to study the initiation of microscale damage and their relationship with dislocation structures, which is a main novelty of this work. This modeling framework provides comprehensive simulations of all aspects of metal AM and offers insights into the dislocation mechanisms and damage formation at microscale in AM materials, which could be used to guide the manipulation of the mechanical properties of AM materials.

Keywords: continuum dislocation dynamics, additive manufacturing, crystal plasticity, phase field damage, finite element method

⋆ Corresponding author: Wentao Yan, pe-mail: mpeyanw@nus.edu.sg

†: Equal contribution

1 Introduction

Metal additive manufacturing (AM) offers not only flexibility in the fabrication of complex structures but also promising potential in the tailoring of the mechanical performance of components [1, 2]. Laser powder-bed-fusion (L-PBF) is a type of metal AM technique that employs laser on powder particles to fabricate parts via melting and solidification [3]. The wide process parameter window of L-PBF allows the design of microstructures and material properties [4, 5]. In L-PBF, the input of laser energy subjects the material to a complex thermal history and significant thermal gradients, which generates substantial thermal stresses in the microstructure during fabrication, introducing dislocation structures that are distinct from conventional manufacturing [6, 7]. The high density dislocation network in AM material has recently been associated with excellent performance, which primarily affects the dislocation motion and the plastic flow under loading [7, 8]. Since the presence of dislocation networks can be beneficial, a significant challenge is to understand how they form during the AM process and how they affect material failure, which is essential to enable the design of material properties in AM.

The motion of dislocations in metals and crystalline materials is a critical phenomenon that leads to plastic deformation, hardening, internal residual stresses and dislocation substructures in mechanical components, which can in turn cause unexpected failures [9, 10]. The relationship between dislocation and microscale damage is complex: on one hand, the motion of dislocations causes plastic deformation and local stress relaxation [11], while on the other hand, the concentration of dislocation lines near obstacles, such as grain boundaries, can lead to pile-ups inducing large stresses that can induce crack initiation [12]. Recent transmission electron microscopy (TEM) experiments show that cellular dislocation structures that form during cyclic fatigue are correlated with the onset of damage near the surface of stainless steel (SS) samples and also cause cyclic softening due to the formation of low dislocation density regions [13, 14, 15]. Crack propagation and dislocation structures are apparently correlated in AM metals, in which crack surfaces have been observed in correspondence with high dislocation density cellular structures [16]. However, the relationship between dislocation structures and damage initiation is not well demonstrated, mainly because of the difficulty of performing interrupted tests to visualize cracking evolution at such a scale, especially in AM materials.

Due to the difficulty of experimentally observing dislocation evolution and micro-crack initiation in AM process, modeling is a promising approach to address this issue. Dislocation dynamics models have already been developed for studying their connection with material behavior, including discrete dislocation dynamics (DDD) [17, 18] and continuous dislocation dynamics (CDD) [19, 20], and are gradually being applied to simulations re-

lated to AM materials [21, 22]. Although researchers have observed intriguing dislocation phenomena in AM materials, there remains very limited research concerning the formation of dislocation structures in the AM process [23, 24]. Dislocation structures such as cells, dislocation walls and persistent slip bands are characteristic of metals that undergo specific thermal and mechanical deformation histories during the manufacturing process. Therefore, to simulate the evolution of dislocation structures during the AM process, capturing both the temperature history and the thermal stress conditions is essential. Our previous work attempted to achieve this through the development of a finite element crystal plasticity modeling framework (CPFE) [25, 26], which revealed the stabilization of dislocations under the combined influence of thermal stresses and temperature in L-PBF 316L SS. However, some important mechanisms are still missing, including cross-slip and climb, thus require a more in-depth investigation by adding specific terms in the constitutive equations. Cross-slip is recognized as necessary to simulate cell structures forming during monotonic loads [27, 28], but this hypothesis has never been tested for the specific thermal stresses that are induced during AM, in which dislocation mobility is temperature dependent. The initial dislocation defects within the material after solidification, which have not been reported yet, could also have a significant impact on the final dislocation state. Moreover, the dislocation evolution leading to microscale damage features is not understood, thus given the micro-mechanics and dislocation phenomena involved, coupling dislocation-based crystal plasticity with damage models is a possible approach to reach a better understanding of the underlying dynamics [29, 30].

The aim of this work is to bridge these gaps by developing a multi-scale, multi-physics modeling framework that reveals the process-structure-property relationship in metal AM, providing insights into dislocation behavior and damage mechanisms at the microscale. This framework uses AM process parameters as input and includes several interconnected models to simulate temperature fields, microstructure, and thermal stress fields, which are then incorporated with a CDD-coupled crystal plasticity model to simulate the evolution of dislocations during the AM process. Additionally, a phase-field model of damage is further incorporated, which is able to model arbitrary damage nucleation and propagation without specifically predetermining their location and direction into the spatial discretization of the model and to study the effect of plastic deformation on damage at the micro-level. The novelty of this modeling framework lies in its ability to comprehensively integrate the models of the AM process, microstructural evolution, thermal stresses, dislocation dynamics and damage. This is used as a tool to understand the relationship between the initiation of microscale damage and dislocation structures formed during the AM process, which should be regarded as a unique aspect that has

not been previously reported. This integration establishes the connection between dislocation structures, microscale damage and process parameters of metal AM, providing a fundamental understanding of AM material properties and their underlying causes from a microscale perspective.

2 Modeling framework and material model

2.1 Overview of the modeling framework for metal AM

In order to comprehensively understand the process-structure-property relationship of metal AM, a multi-scale multi-physics modeling framework is developed. As illustrated in Fig. 1, the framework includes the following sub-models:

- Thermal-fluid flow model: this model can simulate the melt pool dynamics and temperature profiles during the L-PBF process, based on the inputted process parameters, such as laser power, laser scanning speed, powder characteristics and the thermodynamic properties of the material [31]. The outcome temperature data, incorporating both temporal and spatial coordinates, can then be exported to next sub-model.
- Phase field model of grain growth: this model simulates the microstructure evolution during the AM process based on the temperature profiles provided by the thermal-fluid flow model, utilizing thermodynamics and physically-informed parameters. It incorporates the liquid/solid transformation, grain nucleation, and coarsening [32]. The model outputs the grain morphology formed under the specified thermal field, including spatial and orientation information of individual grains, while the orientations can be substituted with EBSD data.
- CPFE thermal stress model: this model, taking the results of the above two models as input, simulates the elastic and plastic deformation, thermal expansion and contraction, and the anisotropic mechanical responses of materials at the grain scale in AM process [25]. Through this model, the evolution and distribution of grain-scale thermal stresses during the AM process can be obtained. Note that the thermal stress model uses a phenomenological CPFE model for plastic deformation on individual slip systems as input for the following dislocation dynamics simulation.
- CDD model coupled with CPFE framework and phase field damage model: this CDD model is coupled with a finite strain crystal plasticity solver, which is based on the original CDD framework by Hochrainer et al. [19]. This model utilizes the deformation and temperature histories of specific grains extracted from the CPFE thermal stress simulations, modeling the motion and formation of dislocation structures on the active slip planes of individual grains under the thermal stresses in AM process [26]. In this

work, the model accounts for dislocation transport, dislocation multiplication and annihilation, dislocation cross-slip, and the evolution of dislocation curvature on a single slip system. The CDD-CPFE model can provide plastic deformation information and stress to the phase field model of damage, which enables the simulation of damage initiation within grains during the AM process.

More details are provided in the following subsections, while the validation and error assessment of each sub-model are evaluated in the Discussion. In particular, the coupling between this framework and the phase field damage model is achieved for the first time, while specific terms to represent double cross slip mechanism are introduced. This modeling framework reveals the process-structure-property relationship of AM to investigate the relationship between AM process-induced deformation, dislocation structures and microscale damage nucleation in AM materials.

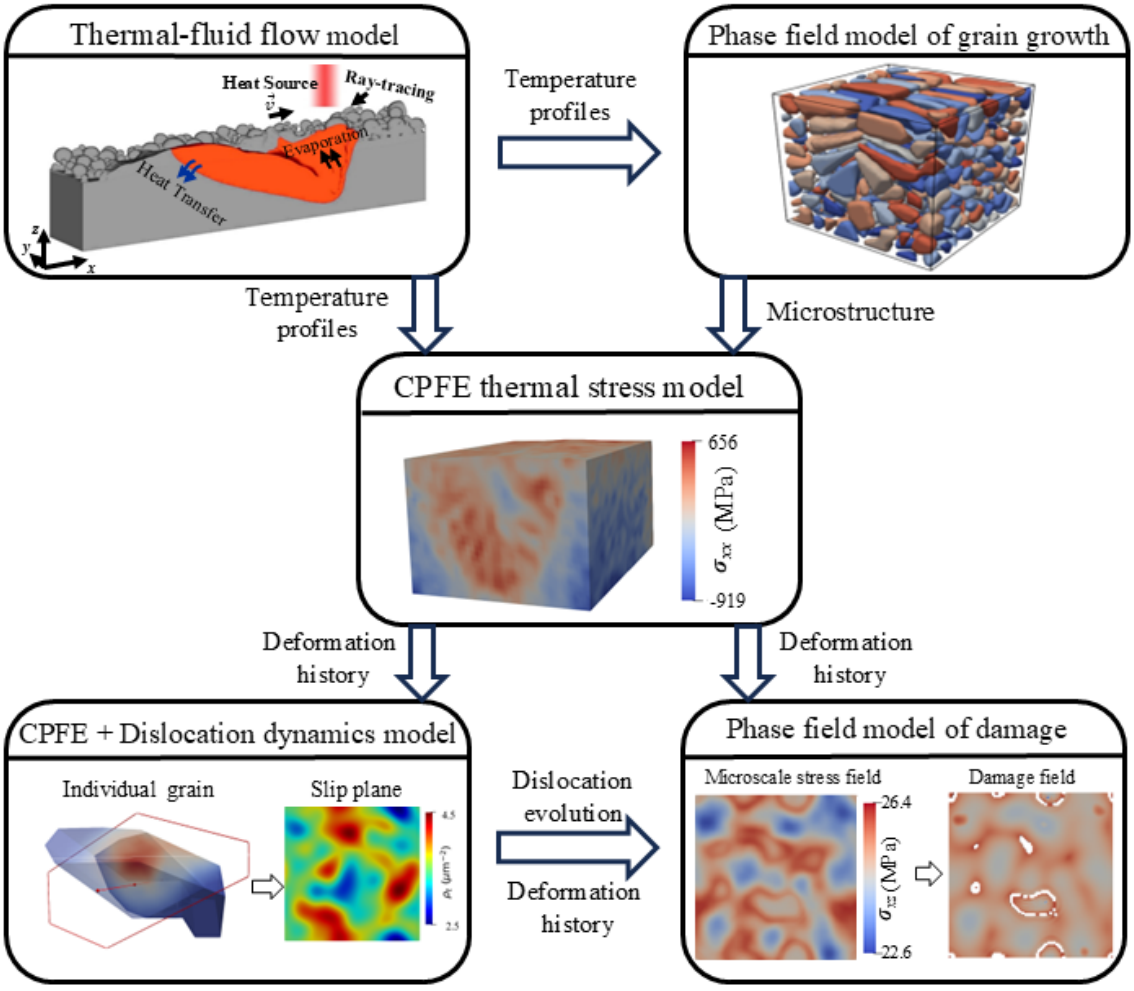

Fig. 1: Multiscale multi-physics modeling framework for the AM process-structure-property relationship.

2.2 Integrative process-structure-property modeling for metal AM

In this section, we present an integrated process-structure-property modeling framework for metal AM, which enables the simulation of the microscale thermal stress evolution during the AM process, serving as a foundation for subsequent dislocation-scale simulations. It is important to note that the models discussed in this section have been detailed in our previous works. However, they are essential prerequisites for the current study, therefore the key information from each model is selected to be presented here.

2.2.1 Thermal-fluid flow model

An accurate temperature field is a necessary starting point for the process-structure-property modeling of AM. In this framework, a multi-physics thermal-fluid flow model is employed, in which the melt pool is simulated as incompressible fluid flow. The governing equations for its continuity, momentum conservation and energy conservation are expressed by [33]:

$$\nabla \cdot \boldsymbol{v} = 0 \ , \tag{1}$$

$$\frac{\partial}{\partial t}(\rho \boldsymbol{v}) + \nabla \cdot (\rho \boldsymbol{v} \otimes \boldsymbol{v}) = -\nabla p + \mu \nabla^2 \boldsymbol{v} + \boldsymbol{f}_b + \rho D \boldsymbol{v} \ , \tag{2}$$

$$\frac{\partial}{\partial t}(\rho e) + \nabla \cdot (\rho e \boldsymbol{v}) = \nabla \cdot (k \nabla T) + Q \ , \tag{3}$$

where ρ is the density of material, μ is the dynamic viscosity, $\boldsymbol{v}$ is the velocity, p is the pressure, T is the temperature, e is the energy, and k represents the thermal conductivity. The buoyancy $\boldsymbol{f}_b$, Darcy drag force $\rho D \boldsymbol{v}$ as well as recoil pressure induced by evaporation, surface tension, heat convection and heat radiation are included. In this model, the laser power is applied at the free surface following a Gaussian distribution. The laser reflection is incorporated by the ray-tracing method, where the energy absorptivity is calculated by Fresnel equation [34]. This model has already been validated in our previous work by comparing the simulated melt pool dimensions with those observed experimentally. For more details, please refer to [31].

2.2.2 Phase field model of grain growth

A three-dimensional phase field model of grain growth is used to generate the grain structure, in which the temperature data from the thermal-fluid flow model above are incorporated as input. This model thoroughly addresses a range of phenomena such as solidification, grain nucleation and growth, competitive grain growth and epitaxial growth originating from powder particles, and grain coarsening within heat affected zones [32].

The grain growth is determined by the Ginzburg-Landau equations [35]:

$$\frac{\partial \zeta(\mathbf{r},t)}{\partial t} = -L_p \frac{\delta F_f\left(\zeta,\eta_i,T\right)}{\delta \zeta(\mathbf{r},t)}, \tag{4}$$

$$\frac{\partial \eta_i(\mathbf{r},t)}{\partial t} = -L_g \frac{\delta F_f\left(\zeta,\eta_i,T\right)}{\delta \eta_i(\mathbf{r},t)}, \tag{5}$$

where $\zeta(\mathbf{r},t)$ represents liquid phase at 0 and represents solid phase at 1, $\eta_i(\mathbf{r},t)$ defines the grain orientation in the i-th grain, L_p is the coefficient for the interfacial mobility and L_g is the kinetic coefficient related to grain boundary. t and T are used to take into account the evolution of time and temperature. F_f is the total free energy given by the integral of the local free energy density f_{local} and the gradient energy density f_{grad} in volume V as $F_f = \int_V \left(f_{\text{local}} + f_{\text{grad}}\right) \mathrm{d}V$. The local free energy includes two parts, f_{phase} and f_{grain}, which represent the free energy density from the liquid/solid phases and from the grains with different orientations, respectively. f_{phase} can be calculated by [32]:

$$f_{\text{phase}} = m_p \left\{(1-\zeta)^2 \times \varphi(\tau) + \zeta^2[1-\varphi(\tau)]\right\}, \tag{6}$$

where m_p is a pre-coefficient, τ is the ratio between T and liquidus temperature, and $\varphi(\tau) = \frac{1}{2}\{1-\tanh[\vartheta \times (\tau-1)]\}$. f_{grain} can be given as [35]:

$$f_{\text{grain}} = m_g \left[\sum_{i=1}^{n}\left(\frac{(\eta_i)^4}{4} - \frac{(\eta_i)^2}{2}\right) + \gamma \sum_{i=1}^{n}\sum_{j\neq i}(\eta_i)^2(\eta_j)^2 + \frac{1}{4} + (1-\zeta)^2 \sum_{i=1}^{n}(\eta_i)^2\right], \tag{7}$$

where m_g is identified as the pre-coefficient, and γ functions as a parameter with the consideration of grain boundary energy and its width. Specifically, the first sum accounts for bulk energy of all grains, the second for the grain boundary energy between grain i and j, while the third accounts for the interaction between the phase fields of all grains and the liquid-solid phase [32]. While the f_{grad} can be given as [35]:

$$f_{\text{grad}} = \frac{\kappa_p}{2}(\nabla\zeta)^2 + \frac{\kappa_g}{2}\sum_{i=1}^{n}(\nabla\eta_i)^2, \tag{8}$$

where κ_p is the gradient coefficient for the liquid/solid interface, and κ_g serves the same purpose for the grain boundary. For anisotropic grain growth with various orientations, a spatial inclination angle φ_{inc} is introduced in the grain boundary energy σ_g [36]:

$$\sigma_g = \sigma_{g_0}\left(1 + \epsilon'\left(\cos^4\varphi_{\text{inc}} + \sin^4\varphi_{\text{inc}}\right)\right), \tag{9}$$

where σ_{g_0} is set as a constant value, while ϵ' is a parameter that determines the extent of anisotropy. The inclination angle is specifically defined by the smallest angle between

the normal direction of grain boundary and the $< 001 >$ orientation. Then the κ_g can be estimated by $\kappa_g = a_k \sigma_g l_g$, where a_k is a coefficient and l_g is the grain boundary width. The heterogeneous grain nucleation based on the Poisson seed method is included to simulate nucleation events on liquid/solid surfaces, which are generated according to the temperature data of the moving melt pool in thermal-fluid flow simulations [37]. The mesh size of this grain growth simulation of AM 316L SS in this work is 1 µm and the time step is 1 µs. This model is able to capture the nucleation and growth of grains during the AM process, which has been validated by comparing with the grain morphology of the as-built AM 316L SS samples [32].

Although the current phase field model of grain growth cannot reproduce the realistic grain structure perfectly, it is already a good solution to reflect the microstructures formed by the temperature fields and melt pool characteristics brought by AM process parameters. In the grain structure generated by the phase field model, each element is assigned a number corresponding to the individual grain it belongs to. This allows the number of each element at its spatial position to be transferred into the CPFE simulation, enabling the identification of the grain structure. After the grains are identified in the simulation domain, the Euler angles obtained from EBSD data of the corresponding AM samples are assigned to the identified individual grains.

Subsequently, the microstructure and temperature fields are input into a phenomenological thermo-mechanical CPFE model to simulate microscale thermal stresses during the AM process. This model has been validated by comparing its predictions with experimental lattice strain results [38]. The thermal stresses obtained from this simulation serve as inputs for the subsequent dislocation dynamics model. To avoid confusion with the dislocation-based CPFE model discussed later, the details, validation, and outputs of this CPFE thermal stress simulation can be found in our previous work [25].

2.3 CDD-CPFE modeling framework for dislocation dynamics in AM process

After obtaining grain-scale thermal stresses from the modeling framework in the previous section, these stress histories can be utilized to study dislocation dynamics within individual grains. In this work, we couple a CDD model with a dislocation-based CPFE model to simulate the formation and evolution of dislocation structures under thermal stresses during the AM process. More details and validation of this CDD-CPFE modeling framework can be found in [26]. Within the dislocation dynamics model, dislocation multiplication and annihilation are considered. For the first time in this study, the cross-slip mechanism is incorporated to enhance the physical to further enhance the physical comprehensiveness and to investigate the effects of various mechanisms and configurations.

2.3.1 Dislocation-based crystal plasticity model

A fully coupled thermo-mechanical dislocation-based crystal plasticity model with finite strain is used in this work. The deformation gradient $\boldsymbol{F}$ can be decomposed into thermal-elastic and plastic parts [39, 40]:

$$\boldsymbol{F} = \boldsymbol{F_e}\boldsymbol{F_p}, \tag{10}$$

where $\boldsymbol{F_e}$ is the thermal-elastic part and $\boldsymbol{F_p}$ is the plastic part. The plastic slip on all slip systems is given as [41]:

$$\boldsymbol{L_p} = \dot{\boldsymbol{F}}_{\boldsymbol{p}}\boldsymbol{F}_{\boldsymbol{p}}^{-1} = \sum_{\alpha=1}^{N_s} \dot{\gamma}^{\alpha}\boldsymbol{m}^{\alpha} \otimes \boldsymbol{n}^{\alpha}, \tag{11}$$

where the vectors $\boldsymbol{m}^{\alpha}$ and $\boldsymbol{n}^{\alpha}$ represent the slip direction unit vector and normal unit vector of slip system α. N_s is the number of slip systems and $\boldsymbol{L_p}$ is the plastic velocity gradient. Here, we primarily introduce the CPFE model coupled with the CDD model for dislocation evolution simulations. A two-way coupling is implemented between these two models: the CPFE framework provides the stress as output, which is used by the CDD as an input to calculate the dislocation velocity and plastic slip rate. On the other hand, the CDD model provides the plastic slip rate as output, which is used by the CPFE framework as an input. The plastic slip rates on the slip systems α are given by [42]:

$$\dot{\gamma} = \rho_t \boldsymbol{v}\boldsymbol{b} \ , \tag{12}$$

where ρ_t is the total dislocation density on slip systems, $\boldsymbol{b}$ is the Burgers vector and v is the dislocation velocity. When the resolved shear stress τ^{α} (RSS) on slip system α exceeds the critical resolved shear stress (CRSS) τ_c^{α}, the dislocation velocity on the slip system α is determined by [43]:

$$\boldsymbol{v}^{\alpha} = B\left(|\tau^{\alpha}| - \tau_c^{\alpha}\right) \mathrm{sign}\left(\tau^{\alpha}\right) \boldsymbol{m}^{\alpha} \ , \tag{13}$$

where B is the dislocation mobility. If the RSS does not exceed the CRSS, the dislocation velocity is set to zero. The RSS is calculated from the 2nd Piola-Kirchhoff stress $\boldsymbol{S}$, which is a function of $\boldsymbol{F_e}$:

$$\boldsymbol{S} = \frac{1}{2}\mathbb{C} : \left(\boldsymbol{F_e^T}\boldsymbol{F_e} - \boldsymbol{I}\right) . \tag{14}$$

The stress is passed from the CPFE framework to the CDD model. The CRSS is calculated by the Taylor hardening equation considering bow-out effect [10, 44]:

$$\tau_c^{\alpha} = \alpha_r G b \sqrt{\rho_t^{\alpha}} + \alpha_b G b / R^{\alpha} \ , \tag{15}$$

where G is the shear modulus, α_r is a coefficient for dislocation motion resistance [45, 46], α_b is the coefficient for the bow-out effect, and R^α is the average radius of curved dislocations given by $R^\alpha = \rho_t^\alpha / q_t^\alpha$ [20], where q_t^α is the total curvature density of the dislocation lines. The temperature dependence of CRSS can be described by [47]:

$$\tau_c^\alpha(T) = (k_A + k_B \cdot \exp[-k_C(T - T_0)]) \cdot \tau_c^\alpha(T_0) \ , \tag{16}$$

where T_0 is the reference temperature, and k_A, k_B and k_C are constants obtained by calibration [25]. Thus the τ_c^α is updated at temperature T with this temperature dependence, and the temperature change would in turn affect the dislocation velocity. Moreover, the temperature dependence of the elasticity tensor can be approximated by a linear function for 316L SS [47]:

$$\mathbb{C}_{ij}(T) = \mathbb{C}_{ij}(T_0) + \frac{\mathrm{d}\mathbb{C}_{ij}}{\mathrm{d}T}(T - T_0) \ . \tag{17}$$

The plastic slip rate calculated in the CDD model by equation (12) is passed to the CPFE framework to calculate the plastic velocity gradient.

2.3.2 Continuum dislocation dynamics model

Four variables are solved for the CDD model, including the total dislocation density ρ_t, two densities ρ_e and ρ_s representing the edge and screw parts of the geometrically necessary dislocation (GND) density, and the total curvature density q_t, which is defined as the density per unit area of the sum of the local curvature of all dislocation segments crossing the unit area [19, 26]. The corresponding differential equations are:

$$\frac{\partial \rho_t}{\partial t} = -\frac{\partial\left(\rho_e \boldsymbol{v}\right)}{\partial x} - \frac{\partial\left(\rho_s \boldsymbol{v}\right)}{\partial y} + \dot{\rho}_{\mathrm{ann}} + \boldsymbol{v} q_t \ , \tag{18}$$

$$\frac{\partial \rho_e}{\partial t} = -\frac{\partial\left(\rho_t \boldsymbol{v}\right)}{\partial x} \ , \tag{19}$$

$$\frac{\partial \rho_s}{\partial t} = -\frac{\partial\left(\rho_t \boldsymbol{v}\right)}{\partial y} \ , \tag{20}$$

$$\begin{aligned} \frac{\partial q_t}{\partial t} = & -\frac{\partial}{\partial x}\left(\frac{\boldsymbol{v}\rho_e q_t}{\rho_t}\right) - \frac{\partial}{\partial y}\left(\frac{\boldsymbol{v}\rho_s q_t}{\rho_t}\right) - \frac{\partial}{\partial x}\left(\frac{\rho_t}{2}\frac{\partial \boldsymbol{v}}{\partial x}\right) - \frac{\partial}{\partial y}\left(\frac{\rho_t}{2}\frac{\partial \boldsymbol{v}}{\partial y}\right) \\ & - \frac{\partial}{\partial x}\left[\frac{(\rho_s^2 - \rho_e^2)}{2\sqrt{\rho_e^2 + \rho_s^2}}\frac{\partial \boldsymbol{v}}{\partial x} - \frac{\rho_e \rho_s}{\sqrt{\rho_e^2 + \rho_s^2}}\frac{\partial \boldsymbol{v}}{\partial y}\right] \\ & - \frac{\partial}{\partial y}\left[-\frac{\rho_e \rho_s}{\sqrt{\rho_e^2 + \rho_s^2}}\frac{\partial \boldsymbol{v}}{\partial x} + \frac{(\rho_e^2 - \rho_s^2)}{2\sqrt{\rho_e^2 + \rho_s^2}}\frac{\partial \boldsymbol{v}}{\partial y}\right] + \dot{q}_{\mathrm{cs}} \ , \end{aligned} \tag{21}$$

where $\boldsymbol{v}$ is the signed dislocation velocity. In equation (18)-(21), the derivatives with respect to x, which is the slip direction, and y, which is the direction of the edge dislocation

line, are calculated in a finite strain framework, i.e., they are calculated with respect to the deformed coordinates. $\dot{\rho}_{\text{ann}}$ and $\dot{q}_{\text{cs}}$ represent the dislocation annihilation rate and the rate of curvature increase due to double cross-slip, respectively. The numerical implementation of the CDD model is detailed in our previous work [26].

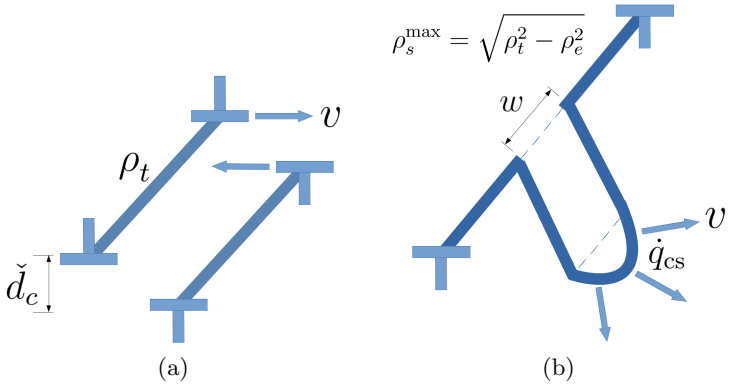

Fig. 2: Schematics of (a) dislocation annihilation and (b) double cross-slip mechanisms.

2.3.3 Implementation of dislocation annihilation and multiplication

In equation (18), $\dot{\rho}_{\text{ann}}$ is the decreasing rate of total dislocation density owing to annihilation, which is used to characterize the annihilation of opposite signed dislocations when the distance between two dislocation lines is less than a characteristic length $\check{d}_c$ [48], as shown in Fig. 2(a). It is to take the effect of dislocation annihilation on the dislocation structures and densities into account, especially in regards to the ratio between high and low dislocation density regions. The annihilation rate can be estimated by approximating the system as a cloud of dislocations with opposite signs traveling towards opposite directions, while the flux, i.e. the dislocation per unit length and unit time is given by $\rho_t |v|$. The cloud of positive dislocations meets the one of negative dislocations and only the dislocations which travel at a distance lower than $\check{d}_c$ are annihilated. Putting together all these considerations, the annihilation rate can be approximated as:

$$\dot{\rho}_{\text{ann}} = -4\check{d}_c\rho_t^2 |v| \ , \tag{22}$$

where the factor 4 stems from the fact that $2\check{d}_c$ is the capture diameter, while another factor 2 is given by the fact that both positive and negative dislocations are traveling towards opposite directions, thus leading to a $2|v|$ relative velocity. The generation of new curvature density, in turn, induces the growth of the total dislocation density because of the term vq_t in equation (18), similar to a Frank-Read source leading to dislocation multiplication [49].

2.3.4 Implementation of dislocation cross-slip

A model for double cross-slip of screw dislocations is utilized to describe the dislocations moving from the primary slip system to a parallel slip plane. This leads to the new dislocation loops generated on the parallel slip plane, as explained in detail in [49]. The purpose of introducing this term is to understand the effect of the curvature increase on the dislocation structure formation. Formulations for the dislocation cross-slip are also added to the rate equations. Even though a single slip system is modelled in the following simulations, double cross-slip causes an increase of the curvature density because of the creation of new dislocation loops, as shown in Fig. 2(b). The $\dot{q}_{\mathrm{cs}}$ in equation (21) is the quantitative increase rate of curvature density caused by double cross-slip. The maximum possible density of screw dislocations is quantified as [26]:

$$\rho_s^{\max} = \sqrt{\rho_t^2 - \rho_e^2} \ , \tag{23}$$

which is necessary because only screw dislocations can cross-slip. Each cross-slip event involves a screw segment with average width w, as shown in Fig. 2(b). For FCC metals, previous atomistic simulations have quantified this width as [49]:

$$w = 44b \ . \tag{24}$$

The cross-slip rate is stress dependent and it has been used in DDD simulations by Depres et al.[50]. Each event generates an additional dislocation loop with curvature radius R_{cs} and the rate of curvature increase can be written as [49, 50]:

$$\dot{\rho}_{\mathrm{cs}} = \frac{w}{L_0 t_0} \cdot \exp\left(\frac{\tau^{\mathrm{cs}} - \tau_{\mathrm{III}}}{k_{Bc}T} V_{act}\right) \cdot \left(\rho_s^+ + \rho_s^-\right) \ , \tag{25}$$

$$\dot{q}_{\mathrm{cs}} = \frac{\beta}{R_{\mathrm{cs}}} \left(\rho_s^+ + \rho_s^-\right) \exp\left(\frac{\left(\tau_{cs} - \tau_{\mathrm{III}}\right) V_{act}}{k_{Bc}T}\right) \ , \tag{26}$$

where τ_{cs} is the RSS on the cross-slip system, V_{act} is the activation volume [50, 51], β is a rate pre-factor [52, 53], T is the temperature and k_{Bc} is the Boltzmann constant. The ρ_s^+ and ρ_s^- are the positive and negative screw dislocation densities, calculated using equations $\rho_s^+ = \frac{1}{2}\left(\sqrt{\rho_t^2 - \rho_e^2} + \rho_s\right)$ and $\rho_s^- = \frac{1}{2}\left(\sqrt{\rho_t^2 - \rho_e^2} - \rho_s\right)$. R_{cs} is approximated as half of the screw dislocation segment that cross-slipped, thus half of $w = 44b$ [54]. L_0 is a reference length that normalizes the cross-slip probability calculation of long dislocations [50], while t_0 is a characteristic time used to normalize the cross-slip probability in time. The inverse of this time is effectively the slip rate. τ_{III} is the stage III stress, which is a threshold stress for the transition to parabolic hardening stage [55] and has been reported

to be linearly dependent on temperature [50, 51]:

$$\tau_{\mathrm{III}}(T) = \tau_{\mathrm{III}}(T_0) + \frac{\mathrm{d}\tau_{\mathrm{III}}}{\mathrm{d}T} \cdot (T - T_0) \ , \tag{27}$$

where the derivative term indicates the change of the stage III stress caused by temperature change. The increase of the dislocation density and curvature density on the parallel cross-slip system is not considered because the simulations are mainly carried out within the primary slip system. The motivation to introduce a rate equation for the double cross-slip mechanism in the present model is to quantitatively understand how such a mechanism affect dislocation structures formation in AM process, which has not been considered yet [26]. The parameters derived from first-principle and DDD studies provide a solid physical basis on the investigation[50, 53]. When including the cross-slip mechanism, the resolved shear stress (RSS) on the cross-slip system τ_{cs} is calculated using the ratio between the Schmid factor on the most active slip system and on the cross-slip system: $\tau_{cs} = \alpha_{cs} \left|\tau^{\alpha}\right|$ and this value is used in equation (26).

Simulations with and without this additional mechanism are carried out to understand its effect on the dislocation structure formation. In this work, dislocation annihilation and double cross-slip are modelled as local mechanisms, i.e. they do not depend on the gradient of the variables, thus no surface term is needed into their weak form.

2.4 Phase field model of damage

The coupling between the phase field model of damage and the crystal plasticity formulation is carried out to describe damage nucleation and propagation in presence of dislocation structures during plastic deformation [56, 57]. A continuum damage variable c between 0 and 1 is used [58]. A value of $c = 0$ represents undamaged material, while $c = 1$ represents completely damaged material, which cannot accommodate stress in tension, as described in the following. A free energy formulation is used, in which the free energy per unit volume includes the mechanical part Ψ_m and the energy released by damage surfaces Ψ_f, regularised as an integral over the volume of the domain Ω [59]:

$$\Psi_f = \int_{\Omega} G_c \gamma(c, \nabla c)\, dV = \int_{\Omega} \frac{G_c}{2} \left(\frac{c^2}{l_0} + l_0 \left|\nabla c\right|^2 \right) dV \ , \tag{28}$$

where G_c is the Griffith's theory critical energy release rate [60], $\gamma(c, \nabla c)$ is the regularised crack energy functional and l_0 is the characteristic regularization length scale, which determines how diffuse the damage field is. In this work, a value to reproduce both nucleation and propagation is adopted, while correlative experimental results of the microscale damage are lacking for calibration [61]. The length scale l_0 can also be used to

calibrate crack nucleation in simulations where pre-existing cracks are not present. This is because the crack nucleation is determined by the ratio G_c/l_0 while G_c alone is the energy release rate during propagation of a pre-existing crack [62, 63, 64]. The fracture nucleation modeling for stainless steel is possible because the ratio G_c/l_0 is calibrated using strain to failure experiments [56, 58].

The mechanical free energy Ψ_m is decomposed into a part a^+, driving the damage evolution, and a part a^-, which does not depend on the damage variable c:

$$\Psi_m = \int_\Omega a \, dV = \int_\Omega \left[(1-c)^2 + k_r\right] a^+ \, dV + \int_\Omega a^- \, dV \ , \tag{29}$$

where k_r is a small residual stiffness, which is necessary for convergence if complete damage has taken place in parts of the representative volume. $a^+ \left(\boldsymbol{F}_e\right)$ and $a^- \left(\boldsymbol{F}_e\right)$ are functions of the elastic deformation gradient $\boldsymbol{F}_e$ and a^- represents the free energy associated with compressive stress states that do not induce damage.

In a finite strain anisotropic medium, an effective bulk modulus K_0 needs to be defined and used:

$$K_0 = \frac{1}{9} \sum_{i,j=1}^{3} \mathbb{C}_{iijj} \ . \tag{30}$$

This is because the elastic energy cannot be decomposed into a part given by the volumetric strain and a part given by the isochoric strain only. The fraction of the mechanical Helmholtz free energy that drives damage is decomposed as:

$$a^+ = a^+_{\text{cpl}} + a^+_{\text{vol}} \ , \tag{31}$$

where a^+_{vol} is the positive volumetric free energy, a^+_{cpl} is the coupled free energy, defined as the difference between the total mechanical free energy of the anisotropic medium and the volumetric part of an equivalent isotropic linear elastic material with bulk modulus K_0. The fraction of the mechanical Helmholtz free energy that does not induce damage is equivalent to the negative volumetric free energy:

$$a^- = a^-_{\text{vol}} \ . \tag{32}$$

This is representative of the fact that volumetric compression does not induce damage in metals. The positive and negative volumetric free energies are:

$$a^+_{\text{vol}} = \begin{cases} \frac{1}{2} K_0 \delta^2 \ , & \text{if } J_e \geq 1 \ , \\ 0 \ , & \text{if } J_e < 1 \ , \end{cases} \tag{33}$$

$$a_{\text{vol}}^{-} = \begin{cases} 0 \ , & \text{if } J_e \geq 1 \ , \\ \frac{1}{2} K_0 \delta^2 \ , & \text{if } J_e < 1 \ , \end{cases} \tag{34}$$

where the elastic volumetric expansion is:

$$\delta = \frac{3}{2} \left(J_e^{2/3} - 1 \right) \ , \tag{35}$$

where $J_e = \det \boldsymbol{F}_e$. The coupled free energy is calculated as:

$$a_{\text{cpl}} = \frac{1}{2} \sum_{i,j=1}^{3} \sum_{k,l=1}^{3} \mathbb{C}_{ijkl} \left(\boldsymbol{E}_e \right)_{ij} \left(\boldsymbol{E}_e \right)_{kl} - \frac{1}{2} K_0 \delta^2 \ , \tag{36}$$

where the Green-Lagrange elastic strain tensor $\boldsymbol{E}_e$ is given by:

$$\boldsymbol{E}_e = \frac{1}{2} (\boldsymbol{F}_e^T \boldsymbol{F}_e - \boldsymbol{I}) = \frac{1}{2} \left(\boldsymbol{C}_e - \boldsymbol{I} \right) \ , \tag{37}$$

where $\boldsymbol{C}_e$ is the right elastic Cauchy-Green tensor and $\boldsymbol{I}$ is the identity matrix. In the small strain formulation, the coupled free energy a_{cpl} corresponds to the free energy contribution of the deviatoric strain. The second Piola-Kirchhoff stress tensor $\boldsymbol{S}$ can be deduced by taking the derivative of the free energy with respect to the Green-Lagrange elastic strain tensor:

$$\boldsymbol{S}_{ij} = \frac{\partial a}{\partial \left(\boldsymbol{E}_e \right)_{ij}} = \begin{cases} [(1-c)^2 + k_r] \sum_{k,l=1}^{3} \mathbb{C}_{ijkl} \left(\boldsymbol{E}_e \right)_{kl} \ , & \text{if } J_e \geq 1 \ , \\ [(1-c)^2 + k_r] \left(\sum_{k,l=1}^{3} \mathbb{C}_{ijkl} \left(\boldsymbol{E}_e \right)_{kl} - J_e^{2/3} K_0 \delta \boldsymbol{C}_e^{-1} \right) + J_e^{2/3} K_0 \delta \boldsymbol{C}_e^{-1} \ , & \text{if } J_e < 1 \ . \end{cases} \tag{38}$$

Note that the stress degradation under a tensile load represents a loss of stiffness, which can be interpreted as the presence of voids in the system and will be passed to the CPFE framework. The evolution of c is determined by the minimization of the sum of the free energies, Ψ_f and Ψ_m. A rate-dependent approach is adopted, based on an Allen-Cahn equation, which ensures the local growth of the damage phase field [65, 66]:

$$\dot{c} = \frac{1}{\eta} \left\langle l_0 \Delta c - \frac{c}{l_0} + 2(1-c) \frac{a^+}{G_c} \right\rangle \tag{39}$$

where η is a kinetic coefficient, and $\langle\rangle$ indicate McCauley brackets, where $\langle x \rangle = x$ if $x > 0$ and $\langle x \rangle = -x$ if $x < 0$. The contribution to damage from both volumetric and isochoric strain is considered because the effect of stress triaxiality is important to determine damage nucleation in metals [61]. Note that the plastic deformation only contributes indirectly and the damage criterion is based on the elastic deformation energy. However,

this formulation is not only applicable to brittle materials but to any material for which fracture can be described with elastic energy-based criteria, which ultimately implies a stress threshold for damage nucleation. Such phase field fracture models have been applied to elasto-plastic materials as summarized by De Lorenzis et al. [67]. The present model belongs to the class of models in which the plastic yield condition does not depend on the damage variable whereas the damage evolution does not depend on the plastic deformation. Our motivation to use this approach is simplicity and the adoption of a purely stress based criterion for damage allows us to investigate the correlation between damage and dislocation density without the complexity of more complex damage criteria.

The hypothesis to test in this work is that the damage field c is correlated with the CDD model variables. The CPFE model is coupled with phase field damage using the MOOSE multiphysics finite element framework [68]. A monolithic solver is used for the stress equilibrium and for the damage evolution, which is based on the preconditioned Jacobian-free Newton-Krylov method and provides an increased computational efficiency [69]. Specifically, the hypre BoomerAMG algebraic multigrid solver is used both as a solver and as a preconditioner [70].

3 Results

3.1 Grain selection and reference simulation

In this work, the parameters for fabricating 316L SS using L-PBF, such as laser power, scanning speed and laser spot size as reported in [25], are input into the thermal-fluid flow simulations to launch the whole modeling framework shown in Fig. 1. The results of thermal stresses are validated by comparing the simulated lattice strain evolutions with those measured by in-situ synchrotron X-ray diffraction experiments [2, 38, 25]. Building upon the previous CPFE simulation of thermal stresses, in which the evolution of microscale residual stresses in the grains can be determined, we can further select individual grains of interest and use the local strain evolution to investigate the dislocation dynamics within them, as depicted in the schematic diagram in Fig. 3. Hereby a grain located beneath the melt pool is selected. This choice is because it has undergone the entire process of laser entering the domain, exiting the domain and cooling stage. Additionally, it is not melted in the whole process, avoiding the argument of dislocation abrupt changes caused by melting and solidification, and instead focusing on the influence of thermal deformation from AM on the dislocation evolution in grains that may have already solidified in the previous cycles. According to the previous study [26], the grains at our selected location have been found to experience the compressive-tensile stress states and develop stable dislocation

Table 1: Model and material parameters used in the simulations

Burgers vector (b) [43]	0.258 nm
Dislocation mobility (B) [44]	0.04 µm/(µs·MPa)
Shear modulus (G) [71]	86 GPa
Dislocation resistance coefficient (α_r) [45]	0.4
Bow-out effect coefficient (α_b) [10]	0.5
Cross-slip resolved shear stress ratio (α_{cs}) [72]	0.33
Maximum dislocation velocity (v_{max}) [26]	0.04 µm/µs
Dislocation annihilation characteristic distance ($\check{d}_c$) [26]	12.8 nm
Pre-factor of double cross-slip (β) [54]	11×10^{-9} µs^{-1}
Characteristic length of a cross-slipping segment (R_{cs}) [72]	5.5 nm
Stage III stress at reference temperature ($\tau_{\mathrm{III}}(T_0)$) [72]	56 MPa
Temperature dependence of stage III stress ($\mathrm{d}\tau_{\mathrm{III}}/\mathrm{d}T$)[72]	-0.02287 MPa/K
Activation volume (V_{act}) [72]	2.8125×10^{-8} µm^3
Residual stiffness coefficient (k_r) [25]	0.01
Boltzmann constant (k_{Bc})	1.3806×10^{-23}m^2·kg/(K·s^2)
Normalization reference length (L_0) [52]	1 µm
Normalization characteristic time (t_0) [52]	1 s
Reference temperature (T_0)	298 K
Temperature dependence of CRSS (k_A) [47]	0.53
Temperature dependence of CRSS (k_B) [47]	0.47
Temperature dependence of CRSS (k_C) [47]	0.008
Elastic constants at $T = T_0$ ($\mathbb{C}_{11}$) [73]	204.6 GPa
Elastic constants at $T = T_0$ ($\mathbb{C}_{12}$) [73]	137.7 GPa
Elastic constants at $T = T_0$ ($\mathbb{C}_{44}$) [73]	126.2 GPa
Derivative of elastic constant ($\mathrm{d}\mathbb{C}_{11}/\mathrm{d}T$) [73]	-90.33 MPa/K
Derivative of elastic constant ($\mathrm{d}\mathbb{C}_{12}/\mathrm{d}T$) [73]	-45.10 MPa/K
Derivative of elastic constant ($\mathrm{d}\mathbb{C}_{44}/\mathrm{d}T$) [73]	-51.78 MPa/K
Volumetric thermal expansion coefficient at T_0 (α_0) [74]	44.73×10^{-6} K^{-1}
Derivative of thermal expansion coefficient (α_1) [75]	0.01011×10^{-6} K^{-2}
Characteristic regularization length scale (l_0)	0.8 µm

structures, making them suitable and representative for further in-depth investigations on the dislocation structure evolution in AM process. Based on the orientation of this selected grain, obtaining its slip systems is straightforward. The dimension of this model is 40µm × 40µm × 0.4µm in x, y and z directions, in which x is along the slip direction $\boldsymbol{m}^\alpha$ and z is along the slip normal direction $\boldsymbol{n}^\alpha$. This model is meshed by hexahedral elements of 0.4 µm. Since the full grain CDD simulations require huge computational cost, a simplified approach is adopted, in which the displacement gradient is spatially projected on the primary activated slip system by using $\boldsymbol{m}^\alpha \cdot \boldsymbol{\nabla u} \cdot \boldsymbol{n}^\alpha$ [26]. The primary activated slip system is obtained by comparing the plastic slip across all the slip systems. The deformation input for CDD simulations is imposed along x direction by projecting the time dependent displacement of the selected grain onto the chosen slip plane as shear deformation, which affects significantly on the dislocation motion. Additionally, the average temperature history of this grain serves as the input for the temperature field. It

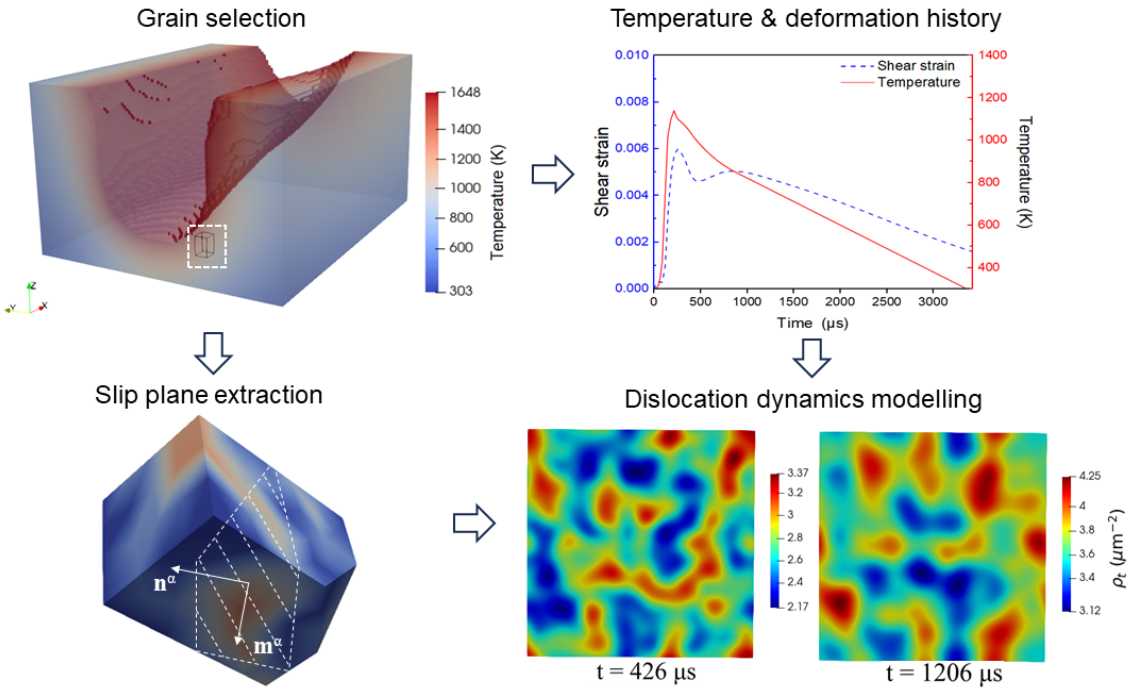

Fig. 3: Schematic of CPFE-CDD modeling: single grain is selected in the thermal stress simulation, in which the most active slip plane is extracted. Incorporating its thermal and deformation histories, the dislocation evolution within this grain is modelled.

can be seen in Fig. 3 that the shear strain on the slip plane is closely related to the thermal process and appears to be non-monotonic in the heating-cooling process, which corresponds to the stress state exchange from compressive to tensile state in the AM process [7].

To initialize the dislocation evolution simulations, hundreds of microscale dislocation loops are randomly assigned on the model. Each of the dislocation loop has a radius of 3 μm and a width of 1 μm. The specific strategy for the initialization is reported in [26]. To provide reference for the following analysis and comparisons, a simulation with the initial density of each dislocation loop set at 0.2 μm^{-2} is conducted in which the cross-slip mechanism and damage model are not incorporated. As shown in the dislocation pattern in Fig. 3, the dislocation structure evolves during the AM process and finally forms a pattern in Fig. 4(a) after cooling down. Based on this, the further impact of different parameters and additional mechanisms can be demonstrated, as discussed in the following sections.

3.2 Effect of initial dislocation configuration

The choice of the initial dislocation configuration affects the final dislocation structures. One significant parameter is the sign of the curvature of the initial dislocation loops. Indeed, each dislocation loop can have a positive or negative curvature, thus ex-

panding or shrinking during positive shear deformation respectively. The simulations of the selected grain are performed with two different initial dislocation distributions, one is initializing 200 dislocation loops with positive curvature, while the other is initializing 130 of the dislocation loops with positive curvature and 70 initial dislocation loops with negative curvature. Each dislocation loop has a peak dislocation density ρ_{init} of 0.2 µm^2. As shown in Fig. 4(a) and (b), even with the same initial dislocation density applied, different signs of curvature result in different dislocation curvature patterns. The comparison between the dislocation structures at the end of the single-layer laser scanning process is shown in Fig. 4. The ratio between ρ_t in high and low-dislocation-density regions is much higher when negatively curved dislocation loops are present at the beginning, as shown in Fig. 4(b). This is due to the source term on the right-hand side of equation (18): negative curvature represents dislocation loops that are shrinking and induces a decrease of the dislocation density in some regions. The surprising result is that the characteristic size of cellular regions is also affected. Indeed, with initial negatively-curved dislocation loops, the resulting cellular structures are visibly larger, as shown in Fig. 4(b).

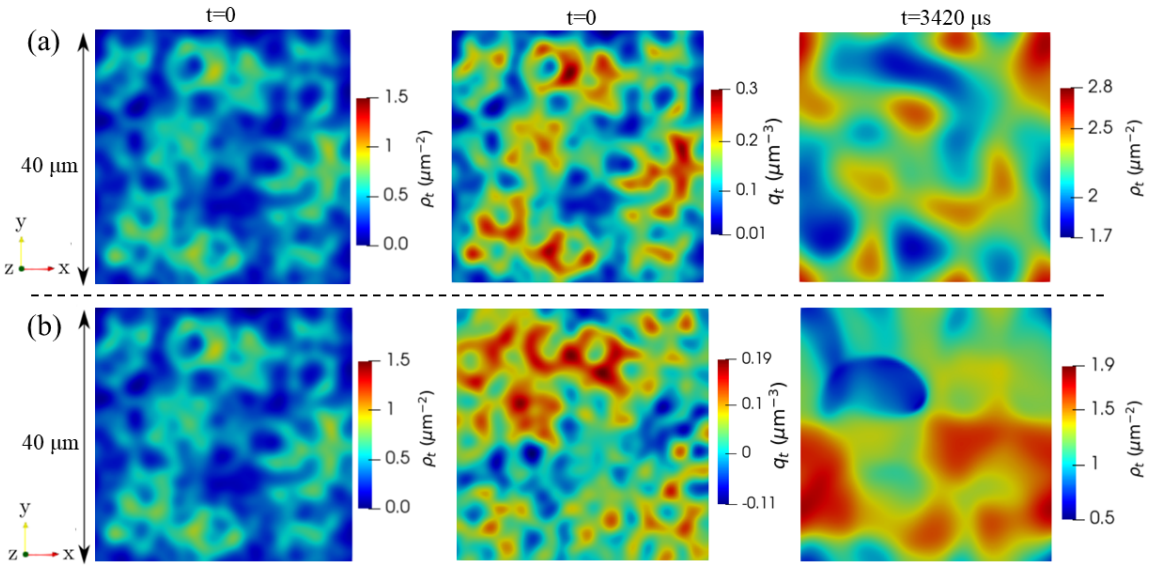

Fig. 4: Initial dislocation density pattern, dislocation curvature pattern and the simulated dislocation evolution at t =3420µs of the selected grain (a) in which all 200 initial dislocation loops have positive curvature and (b) 130 initial dislocation loops have positive curvature, while the other 70 have negative curvature.

In addition, we investigate the effect of the magnitude of the initial dislocation density on simulation results and computational cost. As shown in Table 2, with the increase of the initial dislocation density ρ_{init}, the computational cost increases, showing that the increase of the plastic strain rate due to equation (12) leads to more iterations required to reach convergence. The increase of the average ρ_t is obtained by dividing the final average dislocation density in the representative volume by the initial average dislocation density.

Table 2: Comparison of the simulations with different initial dislocation densities ρ_{init}. Computational times are based on simulations carried out with 12 CPUs.

Initial dislocation loop density ρ_{init} (μm^{-2})	Computation time (h)	Percentage increase of the average ρ_t
0.2	98	537.6%
2	205	203.4%
20	480	119.6%

This reveals how much dislocations move and evolve during the simulations because the dislocation multiplication due to the curvature in equation (18) is proportional to the dislocation velocity. It is evident from Table 2 and Fig. 5 that under the same loading conditions, a lower initial dislocation density exhibits a more significant increase, with a higher degree of dislocation structure evolution. As shown in Fig. 5, although the initial dislocation distribution patterns are the same, and only the peak density of each dislocation loop ρ_{init} is changed, different dislocation structures are obtained at the end of the simulation. This is because given the same plastic deformation, different dislocation densities can affect the travel path length of dislocations. Specifically, higher dislocation density requires lower dislocation motion to accommodate the plastic deformation, as governed by equation (12).

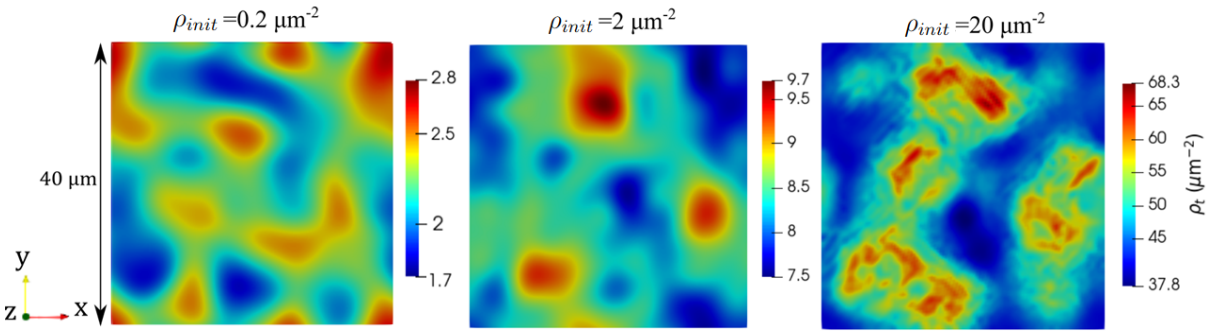

Fig. 5: Final dislocation structures of selected grain with different ρ_{init} for the initial dislocation loops.

3.3 Effect of dislocation cross-slip

Taking the cross-slip mechanism into account in the CDD simulations of the selected grain with ρ_{init}=0.2 μm^{-2}, it can be seen from Fig. 6 that the dislocation structures show significant differences compared with Fig. 3 and Fig. 5. Although this mechanism may not be necessary for dislocation patterning formation and stabilization [26], it may promote dislocation structure formation, as previously reported in other studies [53, 76]. The cross-slip mechanism leads to dislocation density increasing during AM process, attributed to the formation of new dislocation loops during this process. It can be seen from Fig. 6 that

the dislocation density ranges at the same points in time are remarkably higher than those in reference simulation, shown in Fig. 3. In addition, this increase of dislocation loops and density on the slip plane leads to earlier stabilization of the dislocation structure. As shown in Fig. 7, the dislocation velocity decreases to the magnitude of 10^{-3} µm/µs at around 426 µs in the case with cross-slip, and the velocity distribution resembles the pattern of dislocation structure, which implies that the dislocation motion has slowed down to the stage of dislocation structure stabilization. This occurs earlier than that at 660 µs in the reference case, as shown in Fig. 7(a) and as reported in [26]. This result reflects the role of cross-slip mechanism in facilitating the dislocation density evolution during AM process, as well as demonstrating its supportive role in the formation and stabilization of dislocation structures.

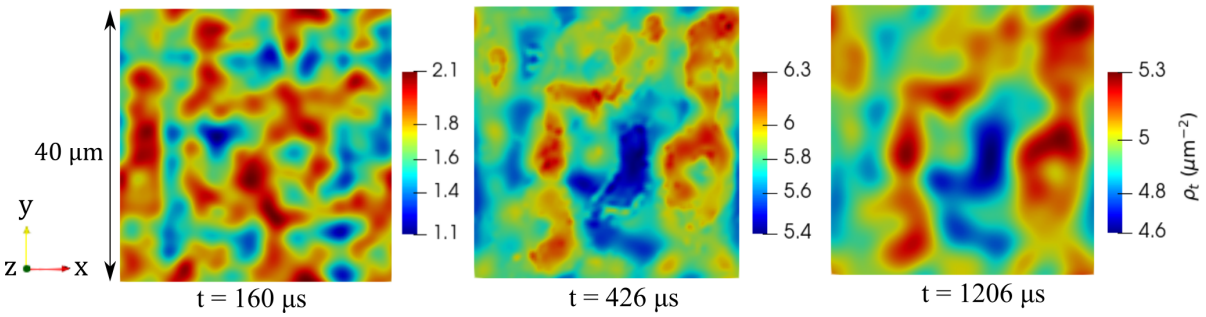

Fig. 6: Dislocation evolution with cross-slip mechanism at different time points.

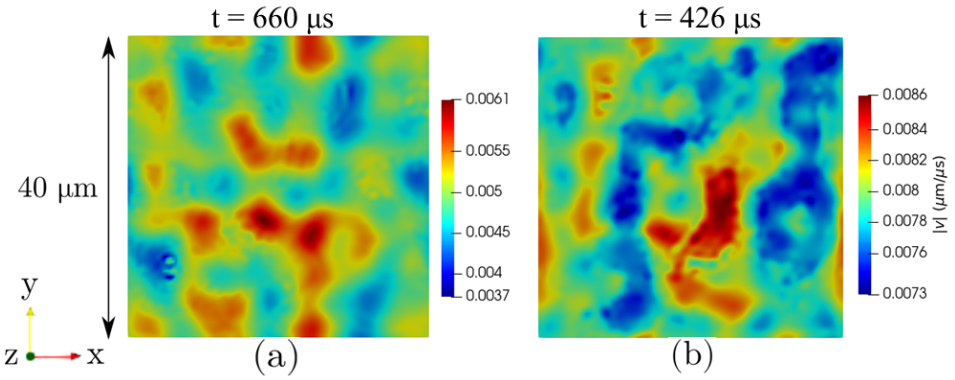

Fig. 7: Comparison of dislocation velocity at the beginning of stabilization of dislocation structure in (a) reference simulation and (b) simulation with cross-slip mechanism.

3.4 Damage under mechanical loading

The thermal loading simulation is carried out for the first 3420 µs in which the deformation from AM process is extracted as the input for the CDD model, as shown in

Fig. 3. Afterwards, an additional unidirectional shear load is applied on the slip plane model to simulate the case in which the AM material is further mechanically loaded. The phase field damage model is introduced in this second step, with a damage energy value of $G_c = 1$ J/m^2. This value is not calibrated but the objective of this simulation work is to demonstrate the correlation between dislocation structures and damage. A different value of G_c would lead to a different strain to failure, but would not invalidate the conclusions reached in this section. As shown in Fig. 8, there is a damage field pattern at the very beginning of the mechanical loading, which is the evolution based on the dislocation structure and reveals the residual deformation from AM process. Indeed, the damage evolution law (39) implies that the presence of residual volumetric and deviatoric elastic strain leads to rapid damage growth. After performing the shear loading for a period to reach the strain amplitude of 1%, it can be found that the pattern of the damage phase field has gradually changed and some new regions with high c value occur on the slip plane. This is attributed to the plastic deformation led by the additional shear load, which requires the dislocation structure to change in order to match the local deformation. The damage field in Fig. 8 has relatively small variations over the representative volume. The first reason is that the model focuses on a relatively small region, with the size of area only 40μm×40μm, which is the characteristic size for damage localization. For instance, the plastic zone ahead of a crack tip in stainless steel will have a characteristic size that is larger than the representative volume used in the present simulation. In the experimental work of Kong et al. [16], micrometer size crack opening and crack length have been observed, whose length scale is comparable with the present simulations. The second reason is that the applied boundary conditions are constraining the system to adopt a more uniform deformation than in a 3D representative volume. The applied boundary condition in this study aims to demonstrate a correlation between dislocation density and damage and does not aim to reproduce larger representative volumes where fracture localizes in a smaller portion of the representative volume. In a larger representative volume and with less constrained boundary conditions, the damage phase field would be more heterogeneous and damage localization would be more evident.

As will be shown in section 3.5, the regions where damage grows during shear loading have a particularly low value of the dislocation density, thus they are regions in which not enough dislocations are available to accommodate the imposed deformation, and the induced stress is higher because more deformation needs to be accommodated by the elastic strain. Further deformation, as shown at time $t = 3530$ μs in Fig. 8, leads to further evolution and growth of the damage phase field. The correlation with respect to

the damage field induced by the residual deformation from AM process (t = 3421 µs) becomes less evident with further deformation.

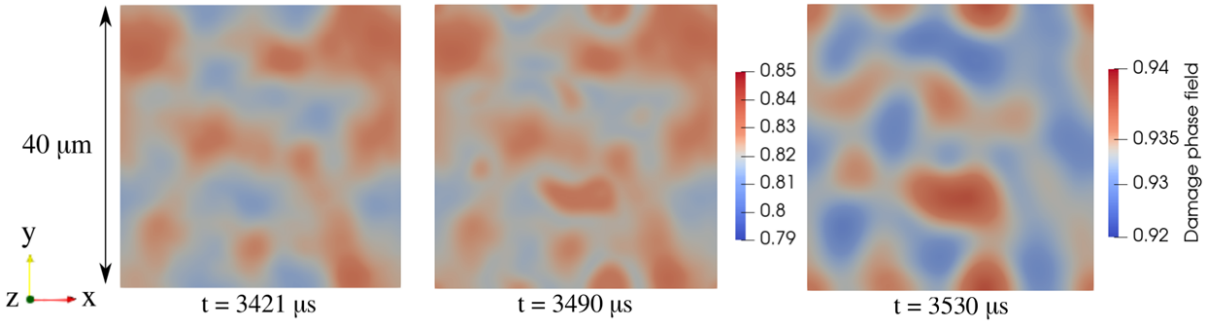

Fig. 8: Damage field at t = 3421 µs just after the AM process, at t = 3490 µs, when the applied shear strain reaches 0.01, and at t = 3530 µs.

3.5 Correlation between damage, plastic deformation and dislocation structures

There is an inherent connection between plastic deformation and damage, and this is closely related to the characteristic of dislocation structures. Here, we select the simulation results at a specific moment (t = 3490 µs) during shear loading in section 3.4 to observe and discuss this correlation. The motivation to choose this time step is related to the load conditions: at t = 3490 µs, the AM process has already taken place, together with an additional shear strain loading, which is useful to assess the effects of the pre-existing dislocation structures, of residual stress and of the plastic deformation during loading. As visible by comparing Fig. 3 with Fig. 9(b), continuing shear loading after the AM process results in a different dislocation structure, where some areas have evolved since the shear loading begins. By correlating it with the damage field in Fig. 9(a), the plastic deformation in Fig. 9(c) and the shear stress field on the slip plane in Fig. 9(d), it can be observed that their patterns show some similarity: specifically, in the regions with higher dislocation density, the shear stress is lower, while the damage phase field has maxima in both regions occupied by dislocation structures and where dislocation density is closer to zero. This similarity can be attributed to the plastic deformation distribution along with the shear loading and dislocation evolution. The component $(\boldsymbol{F}_p)_{xz}$ of the plastic deformation gradient depends on the complex history of the dislocation motion during the AM process and subsequent load, therefore, it correlates, but does not exactly correspond, to the dislocation structures after the AM process and after shear loading. During shear loading, the regions with higher dislocation density can accommodate more plastic deformation, which is due to Orowan law (12), this leads to the correlation between dislocation density and plastic deformation after shear loading, which is evident by comparing

Fig. 9(b) with Fig. 9(c). The lower shear stress in regions with higher dislocation density is therefore associated with the larger accommodation of plastic strain and lower elastic strain. Overall, it can be concluded that the damage field just after the AM process is more correlated with the high dislocation density regions and driven by residual stresses, as revealed in Fig. 9(b) and Fig. 8. By contrast, after further loading, damage starts to grow also in the low dislocation density regions because of increased shear stress on the slip plane.

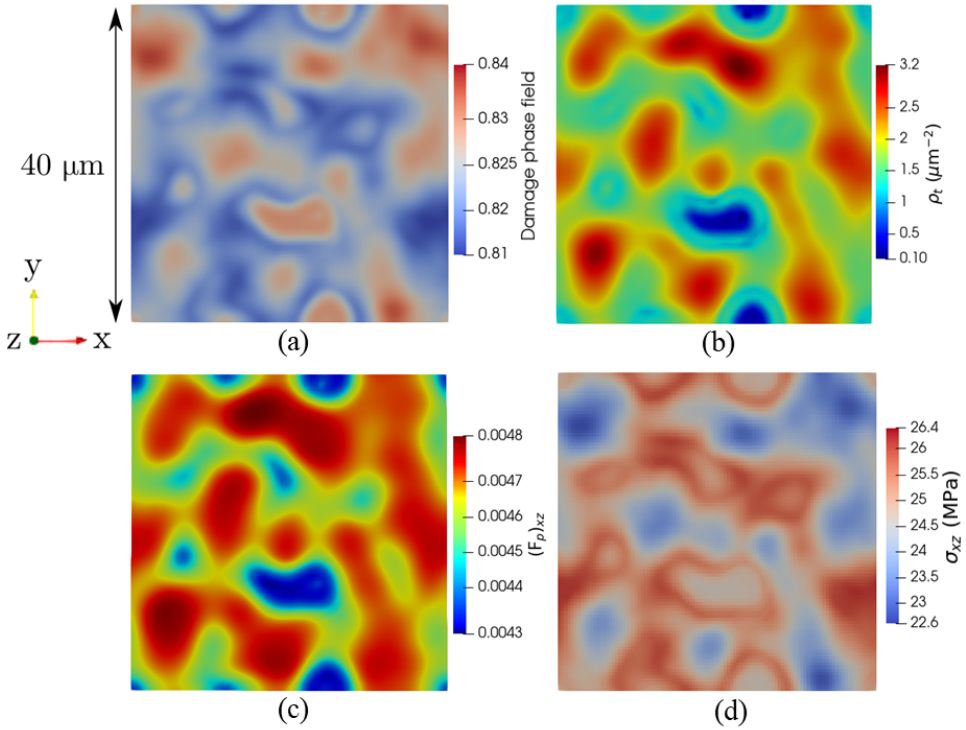

Fig. 9: Simulated patterns on the slip plane under 1% shear loading at 3490 μs: (a) damage phase field, (b) dislocation density ρ_t, (c) plastic deformation component $(F_p)_{xz}$ and (d) shear stress σ_{xz}.

To show the effect of the introduced length scale parameter l_0 in the phase field fracture model, simulations with different values of l_0 are carried out and the results are shown in Fig. 10. The reference simulation in Fig. 9 uses $l_0 = 0.8$ μm. This parametric analysis shows that l_0 plays only a numerical role, while the characteristic pattern of the damage phase field remains the same. The value of l_0 is much smaller than the characteristic size of the dislocation structures reproduced by the current simulations. Therefore, the diffuse nature of the damage phase field shown in Fig. 10 is an intrinsic physical mechanism due to the correlation between dislocation structures and damage, and not a numerical artifact. By comparing Fig.9 with Fig. 10, it is clear that smaller l_0 leads to smaller magnitude of the phase field damage. This is due to the fact that damage nucleation happens when

the elastic energy per unit volume becomes comparable to the characteristic ratio G_c/l_0 [77].

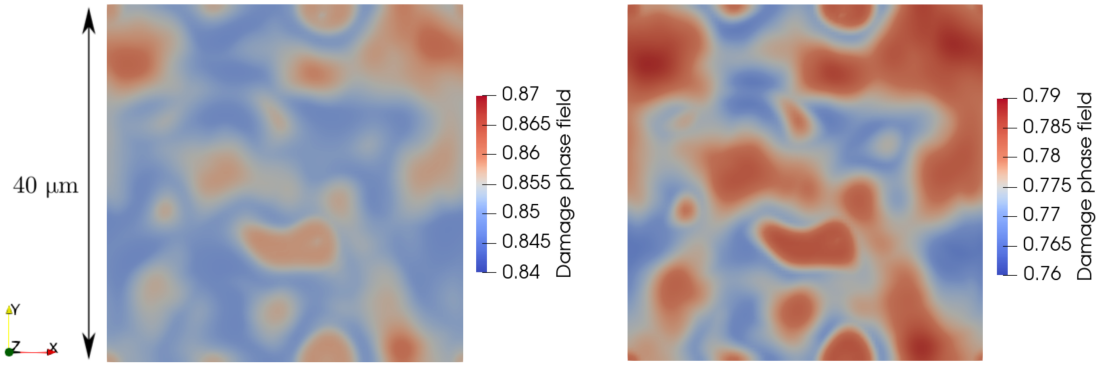

(a) $l_0 = 1$ µm (b) $l_0 = 0.6$ µm

Fig. 10: Pattern of the damage phase field for different values of the length scale parameter l_0 at time $t = 3490$ µs

.

These results reflect a strong correlation between dislocation structures and potential damage, meaning that the regions with higher dislocation density may be more prone to damage. Essentially, under the specified conditions in this work, the accumulation of dislocations resulting from plastic deformation may lead to the occurrence of damage. However, it should be noted that in realistic experiments, there are more factors at play in the materials, rather than solely based on contributions from dislocation and plastic deformation.

4 Discussion

Different initial dislocation configurations should have significant influences on the subsequent dislocation evolution according to section 3.2. Since currently no experiment is able to observe dislocations in the grains immediately after solidification, the present simulations are useful to clarify the dislocation dynamics if different initial dislocation densities are present. As reported in section 3.2, with higher dislocation density after solidification, the dislocation motion is reduced and therefore dislocation multiplication is reduced. For instance, the solidification and cooling parameters can be adjusted for different initial dislocation configurations in AM process to influence the following dislocation structures and following mechanical behaviors. Dislocation structures form anyway but an earlier stabilization of the dislocation structures takes place.

In the high-temperature AM process, dislocation climbing appears to be widely acknowledged as playing a significant role on dislocation dynamics. However, in the highly

transient AM process, the effect of climbing on dislocation velocity remains to be discussed. The velocity of the jog movement can be given by [78, 79]:

$$v_j = \frac{D_s}{k_{Bc}Tb}\left[\sigma b^3 - k_{Bc}T\left(\frac{c}{c_0} - 1\right)\right] \tag{40}$$

where D_s is the coefficient of self-diffusion which decreases with temperature decreasing, σ is the normal stress on the climbing plane, which does not exceed according to our thermal stress simulations. The magnitude of climbing force per unit length of dislocation line $f = \sigma b$. According to [79], by reduction of vacancy formation energy by climbing force on per unit length of dislocation line is fb^2, the equilibrium vacancy concentration becomes:

$$c = c_0 \exp\left(\frac{fb^2}{k_{Bc}T}\right) \ . \tag{41}$$

Substitute all the related values (in table 1 and thermal stress results) into equation (40), v_j is found to be about 450 µm/s in our case at the temperature peak, which is about 12% of the preset max velocity. When the temperature decreases during cooling stage, the climb rate also decreases rapidly, coming from the fact that the self-diffusion coefficient D decreases exponentially as fitted along with the temperature, thus the estimated velocity would decrease to a quite low value very soon, no more than 200 µs. Moreover, the thermal stresses also decrease during the cooling stage, which would lead to the drop of v_j. Therefore in our case this mechanism is not implemented, because the actual climbing rate should be smaller and affect only a short time with limited effect on dislocation velocity. However, it is worth noting that for different AM process parameters and materials, such as those with lower scanning speeds resulting in slower cooling, climbing may play a more remarkable role and need to be further investigated.

The dislocation velocity calculated using equation (13), which is linear with the resolved shear stress, has been previously used in models for cell structure formation using CDD [27, 20]. This is a reasonable approximation because, in the present simulations, the dislocation velocity remains below 0.01 m/s, as shown in Fig. 7, which is the regime in which the stress-velocity relationship can be approximated as linear [10]. The temperature dependence of the CRSS is fitted based on experimental data, a method that has been calibrated in previous work [25]. Although the value of the dislocation mobility B in Table 1 does not depend on temperature, the CRSS is included as temperature dependent, as shown in equation (16). The uncertainty on the dislocation velocity due to the mobility B is not considered in this work because of the specific type of strain-controlled load. In the present simulations, the imposed strain rate on the single slip system determines the dislocation velocity through Orowan's law in equation (12). Thus, the temperature has

only a tiny impact on the dislocation velocity, even though some uncertainty on the stress might be produced. Thermally activated depinning of dislocations will be considered in our future work.

The critical energy release rate G_c is a key factor in phase simulations and it is normally calibrated by comparing microscale simulations with interrupted load experiments that can visualize crack propagation. However, in this work, a precise calibration of G_c is not attempted because of the lack of correlative experiments that combine digital image correlation for strain measurements [80, 81] with damage imaging at the micrometre length scale. Since G_c is material-dependent and influenced by grain orientation [58], which also affects the plastic and thermal deformation in our model, it is challenging to obtain a properly calibrated G_c value for damage modeling on various slip planes. Here, we test how different G_c values from 1 to 100 J/m^2 would affect the damage field under the same loading conditions based on the dislocation structure from the AM process. By comparing the damage fields, it can be observed in Fig. 11 that different G_c values do not result in very different damage patterns because G_c does not significantly change the plastic deformation or dislocation structure, but lead to different c values and ranges on the slip plane. When G_c increases from 1 to 100 J/m^2, the value range of c significantly decreases, which is not conducive to simulating the specific damage field. While the degree of damage varies with different G_c values, under same conditions, smaller G_c values may be more advantageous in deriving the damage information. The proper value of G_c still requires further experimental evidences for reference. At this moment, the same G_c value is applied to compare the effects of other factors on damage in our cases in the Section 3.

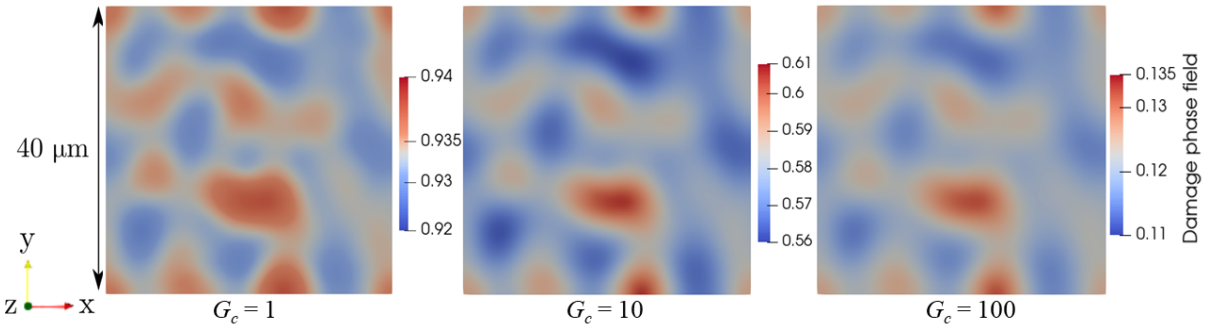

Fig. 11: Damage field on the slip plane model with different G_c values (unit: J/m^2) under same loading at 3530 μs.

The fact that the damage is typically diffuse in the simulations shown in section 3.4 is due to the fact that the shear load is applied directly to one layer of elements, thus limiting the strain heterogeneity that would normally lead to the localization of a single crack. However, the simulation results presented in section 3.5 demonstrate that the

residual deformation induced by the AM process favors damage within high dislocation density regions, which then propagates also to low dislocation density areas during further loading, consistent with the observations in TEM experiments [16].

Since the current modeling framework is a compilation of several models, including the data transfer through multiple stages from AM process to grain growth, thermal stress, dislocation dynamics, and crack initiation, the generation and propagation of errors at each stage should be evaluated. Each model should be independently validated to ensure the effectiveness of result transferred within the framework, and to avoid the 'black box effect' in the entire simulation chain. For the validation of temperature profiles from the thermal-fluid flow model, we compared the melt pool dimensions under identical AM parameters for 316L stainless steel. The discrepancies in width and depth with relative errors not exceeding 9%, demonstrating commendable consistency [32]. As for grain growth, although our model does not fully reproduce the real grain structure as experiment (due to the unpredictability of grain nucleation sites influenced by various factors), it has been validated to reliably yield average grain sizes, numbers and grain aspect ratios consistent with experimental observations, in which the errors are about 10% for these indicators [32]. The grain morphology obtained, combined with grain orientations from EBSD data [38], can adequately support subsequent thermal stress simulations. Measuring thermal stresses at the grain level through experiments is quite challenging. Thus, it is validated by comparing them with residual lattice strains measured using Synchrotron X-ray Diffraction tests [38, 2]. We found that the error did not exceed 0.5×10^{-3} and the simulation was able to predict the elastic-plastic response of different grain families [25]. This indicates that the errors within the simulation chain up to this point are still acceptable. In the thermal stress simulations, cracking phenomena are not considered because the parameters used were optimized in experiments to fabricate crack-free AM 316L SS [2]. However, it is promising that the current method can be extended to the grain scale to address this issue, although significant work is still required to investigate the effect of thermal stresses considering the necessary material parameters and evaluation of the required critical energy.

When it comes to the CDD model, experimentally validating dislocation evolution remains a challenge. The current dislocation model primarily represents behaviors on the main active slip plane within a single grain, but interactions between multiple slip systems and grains can influence the outcome, and the substructure formation in AM materials requires more factors involved. These necessitate further development and increasing computational ability to extend this model. However, the characteristic length scale of the simulated dislocation structures still aligns with the dimensions of some experimen-

tally observed dislocation structures ranging from 6 to 10 µm, which suggests that the current modeling of dislocation structures in AM is reasonable [8, 26, 6]. The ability of this model to predict the evolution of dislocation density has also been evaluated by comparing it with various experimental and simulation results [26, 82, 83], demonstrating good consistency and reliability. The phase field damage model is introduced into the AM-CDD framework for the first time, and currently, there is no direct experimental counterpart for comparison but the effectiveness of this model itself has been previously validated with other metallic materials [58], and crack with similar size was also observed in experimental work in AM stainless steels [16]. More advanced experimental support is expected in the future to help refine and calibrate these models, but current research is grounded in the already validated dislocation structure models, conducted within a reasonable physical framework.. Additionally, it is important to clarify that for the CDD simulations, we did not select grains within the melt pool. This is because, when a grain is melted by the laser into a non-solid state, its deformation and stress are difficult to evaluate, making it challenging to assess whether the extracted deformation history and applied loading are reasonable. Furthermore, there is no clear evidence or experimental evidence regarding the dislocations of a grain immediately after solidification. If an initial dislocation is assigned before the grain melts, it is unreasonable for the high dislocation density resulting from significant deformation during the entire melting process to appear in a newly solidified grain. Thus for grains that undergo the melting-solidification process, the current analysis can be also applied if the simulation starts from the moment after solidification.

Overall, the framework presented in this work demonstrates the ability to simulate the effects of various dislocation mechanisms on potential dislocation structures within individual grains, using validated AM temperature and deformation fields as input. It can be applied to optimize the process parameters to reduce the likelihood of hot cracking and fracture during load by adjusting the thermal stresses. Insights into these microscale mechanisms provide a scientific basis for material selection, process parameter optimization, and post-processing in AM. By adjusting parameters such as laser power, or printing paths, we can effectively influence dislocation formation and evolution, thereby optimizing the properties of final products. The errors in temperature fields, microstructures, and thermal stresses within the model have all been reduced as practically possible using the best state-of-the-art techniques. Furthermore, the models for dislocations and fracture, which are main novelties in the current paper, have also undergone indirect validation. The generation and propagation of errors throughout the entire simulation chain have been assessed in this manner, indicating the framework to be suitable for AM 316L SS,

while it would be adaptable for other AM materials. The correlation between dislocation structures and damage that emerges from the present research is non-trivial because the CDD model is mostly driven by plastic deformation, while the damage model is driven by elastic deformation. Clarifying this correlation was one of the main targets of this research. Despite the comprehensive nature of the proposed models in capturing the complex multiscale phenomena in AM, they are indeed computationally intensive. To address this, various computational acceleration methods could be integrated into the current framework, such as reduced order modeling or hyper-reduction techniques [84, 85, 86], which would offer a promising development for ongoing work by enhancing the simulation efficiency without significantly compromising accuracy. Furthermore, the framework is not fully two-way coupling, for example, the thermal stresses and dislocation pile-up would affect the grain growth or recrystallization [87], which requires further work to make it more physically comprehensive and accurate to help and guide AM fabrication.

5 Conclusion

A multi-scale multi-physics modeling framework is developed to simulate the mechanical response and material behaviors in AM process, covering the process, microstructure and thermal stress behavior, and finally leading to the dislocation evolution and microscale damage in individual grains via the CDD model. In this work, the cross-slip mechanism and the effect of initial dislocation configuration are taken into account. Moreover, a phase field damage model is incorporated in this framework to figure out the correlation between the potential damage and dislocation structure.

The simulation results indicate that the sign of the initial dislocation curvature significantly influences the characteristic size of cellular regions and dislocation motion, while the initial dislocation density affects the amplification of dislocation density under loading. The effects of the cross-slip mechanism during the AM process are discussed for the first time, and it is found to promote the formation and stabilization of dislocation structures, as well as the growth of dislocation density. The damage field on the slip plane is correlated to the residual deformation caused by the AM process. Under subsequent mechanical loading, it continues to evolve based on the as-built pattern, but always in correspondence with the distribution and evolution of shear stress, plastic deformation, and the dislocation structures. This modeling framework presents a qualitative analysis capability for microscale deformation, dislocation motion and damage during the AM process that are difficult to observe experimentally. This research enhances our understanding of dislocation and damage mechanisms induced by thermal stresses in AM process, which provides insights into the dislocation evolution and the initiation of local

microscale cracks in AM materials. Although it still requires further calibration with more experimental data, it can be expected that useful insights into improving the performance of AM materials can be provided via modeling approaches.

6 Acknowledgement

This research is supported by the Ministry of Education, Singapore, under its Academic Research Fund Tier 2 (MOE-T2EP50221-0013), and A*STAR under its Advanced Models for Additive Manufacturing (AM2) programme (Award M22L2b0111). Any opinions, findings and conclusions or recommendations expressed in this material are those of the author(s) and do not reflect the views of the A*STAR.

References

1. Manas V. Upadhyay. On the thermo-mechanical theory of field dislocations in transient heterogeneous temperature fields. *Journal of the Mechanics and Physics of Solids*, 145:104150, 2020.
2. Y Morris Wang, Thomas Voisin, Joseph T McKeown, Jianchao Ye, Nicholas P Calta, Zan Li, Zhi Zeng, Yin Zhang, Wen Chen, Tien Tran Roehling, et al. Additively manufactured hierarchical stainless steels with high strength and ductility. *Nature materials*, 17(1):63–71, 2018.
3. Dirk Herzog, Vanessa Seyda, Eric Wycisk, and Claus Emmelmann. Additive manufacturing of metals. *Acta Materialia*, 117:371–392, 2016.
4. H Wang, ZG Zhu, H Chen, AG Wang, JQ Liu, HW Liu, RK Zheng, SML Nai, S Primig, SS Babu, et al. Effect of cyclic rapid thermal loadings on the microstructural evolution of a CrMnFeCoNi high-entropy alloy manufactured by selective laser melting. *Acta Materialia*, 196:609–625, 2020.
5. Lore Thijs, Karolien Kempen, Jean-Pierre Kruth, and Jan Van Humbeeck. Fine-structured aluminium products with controllable texture by selective laser melting of pre-alloyed alsi10mg powder. *Acta Materialia*, 61(5):1809–1819, 2013.
6. KM Bertsch, G Meric de Bellefon, B Kuehl, and DJ Thoma. Origin of dislocation structures in an additively manufactured austenitic stainless steel 316l. *Acta Materialia*, 199:19–33, 2020.
7. Zan Li, Yinan Cui, Wentao Yan, Di Zhang, Yan Fang, Yujie Chen, Qian Yu, Ge Wang, Heng Ouyang, Chen Fan, et al. Enhanced strengthening and hardening via self-stabilized dislocation network in additively manufactured metals. *Materials Today*, 2021.

8. Leifeng Liu, Qingqing Ding, Yuan Zhong, Ji Zou, Jing Wu, Yu-Lung Chiu, Jixue Li, Ze Zhang, Qian Yu, and Zhijian Shen. Dislocation network in additive manufactured steel breaks strength–ductility trade-off. *Materials Today*, 21(4):354–361, 2018.
9. Nicolò Grilli. *Physics-based constitutive modelling for crystal plasticity finite element computation of cyclic plasticity in fatigue*. PhD thesis, École Polytechnique Fédérale de Lausanne, 2016.
10. Derek Hull and David J Bacon. *Introduction to dislocations*. Butterworth-Heinemann, 2001.
11. Helena Van Swygenhoven. Grain boundaries and dislocations. *Science*, 296(5565):66–67, 2002.
12. A. N. Stroh and Nevill Francis Mott. The formation of cracks as a result of plastic flow. *Proceedings of the Royal Society of London. Series A. Mathematical and Physical Sciences*, 223(1154):404–414, 1954.
13. Duyi Ye, Saburo Matsuoka, Noburo Nagashima, and Naoyuki Suzuki. The low-cycle fatigue, deformation and final fracture behaviour of an austenitic stainless steel. *Materials Science and Engineering: A*, 415(1):104–117, 2006.
14. G. Baudry and A. Pineau. Influence of strain-induced martensitic transformation on the low-cycle fatigue behavior of a stainless steel. *Materials Science and Engineering*, 28(2):229–242, 1977.
15. A. Irastorza-Landa, N. Grilli, and H. Van Swygenhoven. Laue micro-diffraction and crystal plasticity finite element simulations to reveal a vein structure in fatigued cu. *Journal of the Mechanics and Physics of Solids*, 104:157–171, 2017.
16. Decheng Kong, Chaofang Dong, Shaolou Wei, Xiaoqing Ni, Liang Zhang, Ruixue Li, Li Wang, Cheng Man, and Xiaogang Li. About metastable cellular structure in additively manufactured austenitic stainless steels. *Additive Manufacturing*, 38:101804, 2021.
17. S Groh and HM Zbib. Advances in discrete dislocations dynamics and multiscale modeling. *Journal of Engineering Materials and Technology*, 131(4), 2009.
18. Haidong Fan, Alfonso H.W. Ngan, Kefu Gan, and Jaafar A. El-Awady. Origin of double-peak precipitation hardening in metallic alloys. *International Journal of Plasticity*, 111:152–167, 2018.
19. Thomas Hochrainer, Stefan Sandfeld, Michael Zaiser, and Peter Gumbsch. Continuum dislocation dynamics: towards a physical theory of crystal plasticity. *Journal of the Mechanics and Physics of Solids*, 63:167–178, 2014.
20. Stefan Sandfeld and Michael Zaiser. Pattern formation in a minimal model of continuum dislocation plasticity. *Modelling and Simulation in Materials Science and*

Engineering, 23(6):065005, 2015.

21. Kenta Yamanaka, Asumi Kuroda, Miyu Ito, Manami Mori, Huakang Bian, Takahisa Shobu, Shigeo Sato, and Akihiko Chiba. Quantifying the dislocation structures of additively manufactured ti–6al–4v alloys using x-ray diffraction line profile analysis. *Additive Manufacturing*, 37:101678, 2021.
22. Yinan Cui, Kailun Li, Chan Wang, and Wei Liu. Dislocation evolution during additive manufacturing of tungsten. *Modelling and Simulation in Materials Science and Engineering*, 30(2):024001, 2021.
23. Markus Sudmanns, Athanasios P Iliopoulos, Andrew J Birnbaum, John G Michopoulos, and Jaafar A El-Awady. Modeling the evolution of representative dislocation structures under high thermo-mechanical conditions during additive manufacturing of alloys. *Journal of the Mechanics and Physics of Solids*, 179:105367, 2023.
24. Jihye Kwon, G.M. Karthik, Yuri Estrin, and Hyoung Seop Kim. Constitutive modeling of cellular-structured metals produced by additive manufacturing. *Acta Materialia*, 241:118421, 2022.
25. Daijun Hu, Nicolò Grilli, Lu Wang, Min Yang, and Wentao Yan. Microscale residual stresses in additively manufactured stainless steel: Computational simulation. *Journal of the Mechanics and Physics of Solids*, page 104822, 2022.
26. Daijun Hu, Nicolò Grilli, and Wentao Yan. Dislocation structures formation induced by thermal stress in additive manufacturing: Multiscale crystal plasticity modeling of dislocation transport. *Journal of the Mechanics and Physics of Solids*, 173:105235, 2023.
27. S X Xia and A El-Azab. A preliminary investigation of dislocation cell structure formation in metals using continuum dislocation dynamics. *IOP Conference Series: Materials Science and Engineering*, 89(1):012053, jul 2015.
28. Markus Sudmanns, Markus Stricker, Daniel Weygand, Thomas Hochrainer, and Katrin Schulz. Dislocation multiplication by cross-slip and glissile reaction in a dislocation based continuum formulation of crystal plasticity. *Journal of the Mechanics and Physics of Solids*, 132:103695, 2019.
29. Nicolo Grilli, Akshay Dandekar, and Marisol Koslowski. Coupling crystal plasticity and phase-field damage to simulate β-HMX-based polymer-bonded explosive under shock load. In *APS Shock Compression of Condensed Matter Meeting Abstracts*, APS Meeting Abstracts, page Z4.002, June 2017.
30. Nicolò Grilli, Edmund Tarleton, and Alan C.F. Cocks. Neper2cae and pycigen: Scripts to generate polycrystals and interface elements in abaqus. *SoftwareX*, 13:100651, 2021.

31. Lu Wang, Yanming Zhang, and Wentao Yan. Evaporation model for keyhole dynamics during additive manufacturing of metal. *Physical Review Applied*, 14(6):064039, 2020.
32. Min Yang, Lu Wang, and Wentao Yan. Phase-field modeling of grain evolutions in additive manufacturing from nucleation, growth, to coarsening. *npj Computational Materials*, 7(1):1–12, 2021.
33. Wentao Yan, Wenjun Ge, Ya Qian, Stephen Lin, Bin Zhou, Wing Kam Liu, Feng Lin, and Gregory J. Wagner. Multi-physics modeling of single/multiple-track defect mechanisms in electron beam selective melting. *Acta Materialia*, 134:324–333, 2017.
34. Junsu Ahn and Suck-Joo Na. Three-dimensional thermal simulation of nanosecond laser ablation for semitransparent material. *Applied Surface Science*, 283:115–127, 2013.
35. Nele Moelans, Bart Blanpain, and Patrick Wollants. Quantitative analysis of grain boundary properties in a generalized phase field model for grain growth in anisotropic systems. *Physical Review B*, 78(2):024113, 2008.
36. Alain Karma and Wouter-Jan Rappel. Quantitative phase-field modeling of dendritic growth in two and three dimensions. *Physical review E*, 57(4):4323, 1998.
37. J.P Simmons, C Shen, and Y Wang. Phase field modeling of simultaneous nucleation and growth by explicitly incorporating nucleation events. *Scripta Materialia*, 43(10):935–942, 2000.
38. Wen Chen, Thomas Voisin, Yin Zhang, Jean-Baptiste Forien, Christopher M Spadaccini, David L McDowell, Ting Zhu, and Y Morris Wang. Microscale residual stresses in additively manufactured stainless steel. *Nature communications*, 10(1):1–12, 2019.
39. Surya R Kalidindi. Incorporation of deformation twinning in crystal plasticity models. *Journal of the Mechanics and Physics of Solids*, 46(2):267–290, 1998.
40. L Vujošević and VA Lubarda. Finite-strain thermoelasticity based on multiplicative decomposition of deformation gradient. *Theoretical and applied mechanics*, (28-29):379–399, 2002.
41. F. Roters, M. Diehl, P. Shanthraj, P. Eisenlohr, C. Reuber, S.L. Wong, T. Maiti, A. Ebrahimi, T. Hochrainer, H.-O. Fabritius, S. Nikolov, M. Friák, N. Fujita, N. Grilli, K.G.F. Janssens, N. Jia, P.J.J. Kok, D. Ma, F. Meier, E. Werner, M. Stricker, D. Weygand, and D. Raabe. Damask – the Düsseldorf advanced material simulation kit for modeling multi-physics crystal plasticity, thermal, and damage phenomena from the single crystal up to the component scale. *Computational Materials Science*, 158:420 – 478, 2019.
42. Symposium on internal stresses in metals and alloys. *Nature*, 164:296–296, 1949.

43. Shengxu Xia and Anter El-Azab. Computational modelling of mesoscale dislocation patterning and plastic deformation of single crystals. *Modelling and Simulation in Materials Science and Engineering*, 23(5):055009, 2015.
44. MS Pham, SR Holdsworth, KGF Janssens, and Edoardo Mazza. Cyclic deformation response of aisi 316l at room temperature: mechanical behaviour, microstructural evolution, physically-based evolutionary constitutive modelling. *International Journal of Plasticity*, 47:143–164, 2013.
45. Athanasios Arsenlis and David M. Parks. Modeling the evolution of crystallographic dislocation density in crystal plasticity. *Journal of the Mechanics and Physics of Solids*, 50(9):1979–2009, 2002.
46. N. Grilli, K.G.F. Janssens, J. Nellessen, S. Sandlöbes, and D. Raabe. Multiple slip dislocation patterning in a dislocation-based crystal plasticity finite element method. *International Journal of Plasticity*, 100:104–121, 2018.
47. MR Daymond and PJ Bouchard. Elastoplastic deformation of 316 stainless steel under tensile loading at elevated temperatures. *Metallurgical and Materials transactions A*, 37(6):1863–1873, 2006.
48. Franz Roters, Dierk Raabe, and Günter Gottstein. Work hardening in heterogeneous alloys—a microstructural approach based on three internal state variables. *Acta materialia*, 48(17):4181–4189, 2000.
49. Nicolò Grilli, Koenraad GF Janssens, and Helena Van Swygenhoven. Crystal plasticity finite element modelling of low cycle fatigue in fcc metals. *Journal of the Mechanics and Physics of Solids*, 84:424–435, 2015.
50. Christophe Déprés. *Modélisation physique des stades précurseurs de l'endommagement en fatigue dans l'acier inoxydable austénitique 316L.* PhD thesis, Grenoble INPG, 2004.
51. J Bonneville, B Escaig, and JL Martin. A study of cross-slip activation parameters in pure copper. *Acta Metallurgica*, 36(8):1989–2002, 1988.
52. Marc Fivel. Etudes numériques à différentes échelles de la déformation plastique des monocristaux de structure cfc. *These de Doctorat, Université Joseph Fourier-Grenoble*, 1997.
53. Shengxu Xia, James Belak, and Anter El-Azab. The discrete-continuum connection in dislocation dynamics: I. time coarse graining of cross slip. *Modelling and Simulation in Materials Science and Engineering*, 24(7):075007, 2016.
54. B Escaig. Sur le glissement dévié des dislocations dans la structure cubique à faces centrées. *Journal de Physique*, 29(2-3):225–239, 1968.

55. C Robertson, MC Fivel, and A Fissolo. Dislocation substructure in 316l stainless steel under thermal fatigue up to 650 k. *Materials Science and Engineering: A*, 315(1-2):47–57, 2001.
56. Michael Salvini, Nicolò Grilli, Eralp Demir, Siqi He, Tomas Martin, Peter Flewitt, Mahmoud Mostafavi, Christopher Truman, and David Knowles. Effect of grain boundary misorientation and carbide precipitation on damage initiation: A coupled crystal plasticity and phase field damage study. *International Journal of Plasticity*, 172:103854, 2024.
57. Tomas Martin, Siqi He, Edward Horton, Hao Shang, Antonio Fernandez-Caballero, Nicolo Grilli, Mahmoud Mostafavi, David Knowles, Alan Cocks, and Peter Flewitt. New correlative microscopy approaches to understand the microstructural origins of creep cavitation in austenitic steels. *Microscopy and Microanalysis*, 28(S1):2074–2075, 2022.
58. Nicolò Grilli and Marisol Koslowski. The effect of crystal anisotropy and plastic response on the dynamic fracture of energetic materials. *Journal of Applied Physics*, 126(15):155101, 2019.
59. Nicolò Grilli and Marisol Koslowski. The effect of crystal orientation on shock loading of single crystal energetic materials. *Computational Materials Science*, 155:235 – 245, 2018.
60. Alan Arnold Griffith and Geoffrey Ingram Taylor. Vi. the phenomena of rupture and flow in solids. *Philosophical Transactions of the Royal Society of London. Series A, Containing Papers of a Mathematical or Physical Character*, 221(582-593):163–198, 1921.
61. Michael J. Borden, Thomas J.R. Hughes, Chad M. Landis, Amin Anvari, and Isaac J. Lee. A phase-field formulation for fracture in ductile materials: Finite deformation balance law derivation, plastic degradation, and stress triaxiality effects. *Computer Methods in Applied Mechanics and Engineering*, 312:130–166, 2016.
62. Xuejian Ding, Jiejiang Zhao, Hao Huang, Shurong Ding, and Yongzhong Huo. Effect of damage rate on the kinetics of void nucleation and growth by phase field modeling for materials under irradiations. *Journal of Nuclear Materials*, 480:120–128, 2016.
63. Stella Brach, Erwan Tanné, Blaise Bourdin, and Kaushik Bhattacharya. Phase-field study of crack nucleation and propagation in elastic–perfectly plastic bodies. *Computer Methods in Applied Mechanics and Engineering*, 353:44–65, 2019.
64. Camilo A. Duarte, Nicolò Grilli, and Marisol Koslowski. Effect of initial damage variability on hot-spot nucleation in energetic materials. *Journal of Applied Physics*, 124(2):025104, 2018.

65. C. Miehe, F. Welschinger, and M. Hofacker. Thermodynamically consistent phase-field models of fracture: Variational principles and multi-field fe implementations. *International Journal for Numerical Methods in Engineering*, 83(10):1273–1311, 2010.
66. Michael N. Sakano, Ahmed Hamed, Edward M. Kober, Nicolo Grilli, Brenden W. Hamilton, Md Mahbubul Islam, Marisol Koslowski, and Alejandro Strachan. Unsupervised learning-based multiscale model of thermochemistry in 1,3,5-trinitro-1,3,5-triazinane (rdx). *The Journal of Physical Chemistry A*, 124(44):9141–9155, 2020.
67. R. Alessi, M. Ambati, T. Gerasimov, S. Vidoli, and L. De Lorenzis. *Comparison of Phase-Field Models of Fracture Coupled with Plasticity*, pages 1–21. Springer International Publishing, Cham, 2018.
68. Cody J. Permann, Derek R. Gaston, David Andrš, Robert W. Carlsen, Fande Kong, Alexander D. Lindsay, Jason M. Miller, John W. Peterson, Andrew E. Slaughter, Roy H. Stogner, and Richard C. Martineau. Moose: Enabling massively parallel multiphysics simulation. *SoftwareX*, 11:100430, 2020.
69. K. Chockalingam, M. R. Tonks, J. D. Hales, D. R. Gaston, P. C. Millett, and Liangzhe Zhang. Crystal plasticity with jacobian-free newton–krylov. *Computational Mechanics*, 51(5):617–627, 2013.
70. Robert D. Falgout and Ulrike Meier Yang. hypre: A library of high performance preconditioners. In Peter M. A. Sloot, Alfons G. Hoekstra, C. J. Kenneth Tan, and Jack J. Dongarra, editors, *Computational Science — ICCS 2002*, pages 632–641, Berlin, Heidelberg, 2002. Springer Berlin Heidelberg.
71. ES Puchi Cabrera. High temperature deformation of 316l stainless steel. *Materials science and technology*, 17(2):155–161, 2001.
72. Christophe Déprés, CF Robertson*, and MC Fivel. Low-strain fatigue in aisi 316l steel surface grains: a three-dimensional discrete dislocation dynamics modelling of the early cycles i. dislocation microstructures and mechanical behaviour. *Philosophical Magazine*, 84(22):2257–2275, 2004.
73. B. Clausen, T. Lorentzen, and T. Leffers. Self-consistent modelling of the plastic deformation of F.C.C. polycrstals and its implications for diffraction measurements of internal stresses. *Acta Materialia*, 46(9):3087–3098, 1998.
74. Ainara Irastorza-Landa, Nicolò Grilli, and Helena Van Swygenhoven. Effect of pre-existing immobile dislocations on the evolution of geometrically necessary dislocations during fatigue. *Modelling and Simulation in Materials Science and Engineering*, 25(5):055010, may 2017.
75. Wenchun Jiang, Yucai Zhang, and Wanchuck Woo. Using heat sink technology to decrease residual stress in 316l stainless steel welding joint: Finite element simulation.

International journal of pressure vessels and piping, 92:56–62, 2012.

76. Z Q Wang, I J Beyerlein, and R LeSar. The importance of cross-slip in high-rate deformation. *Modelling and Simulation in Materials Science and Engineering*, 15(6):675–690, sep 2007.
77. Aditya Kumar, Blaise Bourdin, Gilles A. Francfort, and Oscar Lopez-Pamies. Revisiting nucleation in the phase-field approach to brittle fracture. *Journal of the Mechanics and Physics of Solids*, 142:104027, 2020.
78. G Edelin. On dislocation climb rate. *The Philosophical Magazine: A Journal of Theoretical Experimental and Applied Physics*, 23(186):1547–1550, 1971.
79. Jun-Shan Zhang. *High temperature deformation and fracture of materials*. Elsevier, 2010.
80. Nicolò Grilli, Philip Earp, Alan C.F. Cocks, James Marrow, and Edmund Tarleton. Characterisation of slip and twin activity using digital image correlation and crystal plasticity finite element simulation: Application to orthorhombic -uranium. *Journal of the Mechanics and Physics of Solids*, 135:103800, 2020.
81. Dylan Agius, Anna Kareer, Abdullah Al Mamun, Christopher Truman, David M. Collins, Mahmoud Mostafavi, and David Knowles. A crystal plasticity model that accounts for grain size effects and slip system interactions on the deformation of austenitic stainless steels. *International Journal of Plasticity*, 152:103249, 2022.
82. M.S. Pham, C. Solenthaler, K.G.F. Janssens, and S.R. Holdsworth. Dislocation structure evolution and its effects on cyclic deformation response of aisi 316l stainless steel. *Materials Science and Engineering: A*, 528(7):3261–3269, 2011.
83. Dongsheng Li, Hussein Zbib, Xin Sun, and Mohammad Khaleel. Predicting plastic flow and irradiation hardening of iron single crystal with mechanism-based continuum dislocation dynamics. *International Journal of Plasticity*, 52:3–17, 2014. In Honor of Hussein Zbib.
84. Zeliang Liu, Orion L Kafka, Cheng Yu, and Wing Kam Liu. Data-driven self-consistent clustering analysis of heterogeneous materials with crystal plasticity. *Advances in Computational Plasticity: A Book in Honour of D. Roger J. Owen*, pages 221–242, 2018.
85. Ye Lu, Kevontrez Kyvon Jones, Zhengtao Gan, and Wing Kam Liu. Adaptive hyper reduction for additive manufacturing thermal fluid analysis. *Computer Methods in Applied Mechanics and Engineering*, 372:113312, 2020.
86. Lei Zhang, Ye Lu, Shaoqiang Tang, and Wing Kam Liu. Hidenn-td: Reduced-order hierarchical deep learning neural networks. *Computer Methods in Applied Mechanics and Engineering*, 389:114414, 2022.

87. Pu Deng, Houshang Yin, Miao Song, Dian Li, Yufeng Zheng, Barton C Prorok, and Xiaoyuan Lou. On the thermal stability of dislocation cellular structures in additively manufactured austenitic stainless steels: roles of heavy element segregation and stacking fault energy. *Jom*, 72(12):4232–4243, 2020.